PORTUGALIAE PHYSICA

VOLUME 20

1989 / 91

SOCIEDADE PORTUGUESA DE FÍSICA

PORTUGALIAE PHYSICA

Fundada em 1943 por A. Cyrillo Soares, M. Telles Antunes, A. Marques da Silva e M. Valadares

Director

J. M. Machado da Silva (Faculdade de Ciências, Universidade do Porto)

Co-Directores

M. Salete Leite (Faculdade de Ciências, Universidade de Coimbra)

Alexandre Quintanilha (ICBAS, Universidade do Porto)

Comissão Redactorial

B. Barbara (Laboratório Louis Néel, CNRS — Grenoble)

Kim Carneiro (Instituto Dinamarquês de Metrologia. Lingby)

F. Bragança Gil (Faculdade de Ciências, Universidade de Lisboa)

I. R. Harris (Departamento de Metalurgia, Universidade de Birmingham)

M. Salete Leite (Faculdade de Ciências, Universidade de Coimbra)

N. Miura (Instituto de Física do Estado Sólido, Universidade de Tokyo)

M. Ida (Faculdade de Ciências, Universidade de Kobe)

F. D. Santos (Faculdade de Ciências, Universidade de Lisboa)

J. Machado da Silva (Faculdade de Ciências, Universidade do Porto)

J. B. Sousa (Faculdade de Ciências, Universidade do Porto)

R. Stinchcombe (Departamento de Física Teórica, Universidade de Oxford)

M. Velarde (Faculdade de Ciências, UNED — Madrid)

J. P. Burger (Université de Paris, Orsay)

F. R. N. Nabarro (University of Witwatersrand, Johannesburg)

Anteriores Directores

A. Cyrillo Soares (1943-1949), A. Monteiro (1951-1954)

A. da Silveira (1965-1975), J. M. Araújo (1979-1986)

Publicação subsidiada pelo INSTITUTO NACIONAL DE INVESTIGAÇÃO CIÊNTÍFICA

ISSN 0048 - 4903

PORTUGALIAE PHYSICA

VOLUME 20

1989 / 91

117

Letter from the Editor

The publication of Portugaliae Physica has been discontinued for some time to allow for a change in format. We regret that this has taken longer than we expected. The format has been changed to that of two columns per page and we now have the journal processed by computer. This will speed up its publication and make it possible for would be authours to submit their papers in a diskette. The articles submited will be, as before, sent to referees and if accepted they will be published in due course.

THE FLUIDITY OF WATER AT LIPID-WATER INTERFACES JUST BELOW 0 C

ALBERTO M. S. C. AMARAL[1], ANA MARGARIDA DAMAS[2] , ALEXANDRE QUINTANILHA[3]
[1]Departamento de Química, Faculdade de Ciências, [2]Sector de Biofísica,I.C.B.A.S.,Universidade do Porto, 4000 Porto, Portugal, and [3]Department of Physiology-Anatomy, U.C. Berkeley, CA 94720, USA

ABSTRACT -Using several different electron paramagnetic probes we have studied the phase transitions of two lipids with transition temperatures both well above and well below 0 C in lipid-water mixtures: we show that about 20-25 moles of water per mole of lipid will remain in a fluid state just below 0 C only if the lipid is already in the gel state (i.e. below its phase transition temperature).

1.INTRODUCTION

Previous studies of hydrated lipid-systems using calorimetry [1,2], deuteron magnetic resonance [3-5] and electron spin resonance(ESR) [6] have revealed that as many as 21 moles of water per mole of lipid have their mobility restricted and can be distinguished from bulk water. Part of this water (usually less than 10 moles per mole of lipid) is strongly immobilized and is referred to as "bound" water [7]. It has been suggested [1] that this "bound" water forms a complex hydrate structure around the polar group of the lipid.

We have used electron paramagnetic probes to study the fluidity of lipid-water systems, using lipids with transition temperatures both above and below 0 C. The experimental evidence obtained suggests that the amount of non-freezable water at or just below the freezing point of the bulk water is strongly dependent on the fluidity state of the lipid phase.

2.MATERIALS AND METHODS

A Varian E-109 X-band electron spin resonance spectrometer with a Varian E-257 variable temperature controller (allowing the control of temperature at the sample within less than 0.5 C) was used. Temperatures were checked with a thermocouple inserted into similar micropipets as those used as sample holders and placed in the magnetic cavity; temperature changes were stabilized within 1-2 minutes. Dimyristoyl phosphatidylcholine (DMPC) and Dioleoyl phosphatidylcholine (DOPC) were the two lipids chosen since they had transition temperatures well above (+23 C for DMPC) and well below (-20 C for DOPC) the freezing temperature of bulk water. They were purchased from Sigma Chemical Co. (Poole, England). The neutral paramagnetic probes 2,2,6,6-tetramethylpiperidone-4-oxyl (Tempone), 2,2,6,6 - tetramethylpiperidine - N - oxyl (Tempo) and the cationic probe 4-nonyldimethyl ammonium -1 - oxyl -

(2,2,6,6-tetramethyl-piperidine) bromide (CAT_9) were provided by Dr. R.J. Mehlhorn.

Lipid-water mixtures were prepared under nitrogen using standard techniques [6] at an approximate molar ratio of 80 moles of water per mole of lipid and containing 0.125 mM paramagnetic probe (corresponding to roughly 1 mole of probe per 4000 moles of lipid). Samples of 50 microlitres were placed in micropipets (that had been thoroughly flushed with nitrogen) which were then sealed to prevent the subsequent entry of oxygen (this is particularly important if we wish to minimize lipid peroxidation). ESR spectra were recorded at temperatures in the range between +30 C and -60 C. Spectra of the same paramagnetic probes dissolved in water alone were also recorded across the same temperature profile. The viscosity of the medium in which the probe is located is proportional to the correlation time t given by:

$$t=6.5*10^{-10}\,\Delta H_0[(h_0/h_{-1})^{1/2}-1]$$

where h_{-1} and h_o are the heights of the high field and central lines of the ESR spectrum and ΔH_o is the line width of the central line in Gauss [6].

3. RESULTS AND DISCUSSION

Fig. 1 shows a series of spectra obtained from the system DMPC-water, using the paramagnetic probe Tempo at the indicated temperatures. At 25 C the lipid is still in the fluid state (as we are still above the transition temperature for this lipid) and most of the paramagnetic probe can be seen to be located in the lipid phase. As the temperature is lowered past 23 C (the transition temperature for this lipid) the probe is progressively excluded from the gel lipid phase such that most of it is now to be found in the liquid water phase. When this lipid-water

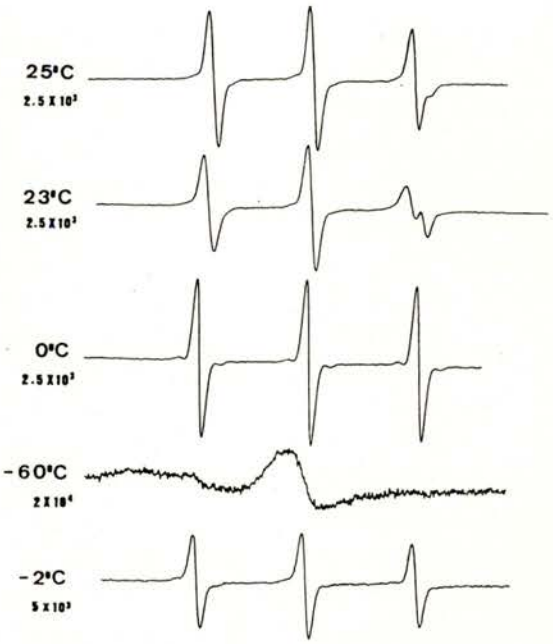

Figure 1 - ESR spectra of the nitroxide spin probe Tempo in DMPC-Water systems at the indicated temperatures and gains.

system is cooled to -60 C the observed signal is one that is characteristic of the strong immobilization of the probe that is to be expected from it being trapped in frozen water. In the DMPC-water system

the hyperfine splitting of spectral lines is approximately 17.40 Gauss for the probe in the liquid water, and 16.05 Gauss for the probe in the fluid lipid environment respectively. Upon heating from -60 C to -2 C and then further to 0 C (and waiting about 15 minutes for the spectra to stabilize for each temperature) we observe only one freely mobile population of probe with a hyperfine splitting constant of 17.35 Gauss characteristic of its presence in an aqueous environment. While accurate quantification is problematic, if one assumes that well below the phase transition of this lipid (23 C) most of the probe is to be found in the aqueous environment, then the spectrum taken at -2 C suggests that the amount of fluid water is approximately 25% of the total water; this means that 20-25 moles of water per mole of lipid remain unfrozen at -2 C. Data of Salsbury et al [4] have shown quite clearly that as many as 21 moles of water per mole of lipid have their motion restricted in some manner; more recent data indicate some solutes, like sucrose, will affect the amount of unfrozen water [8].

Fig. 2 displays representative spectra obtained for the DOPC-water system with the same paramagnetic probe Tempo at several temperatures. At 0 C DOPC is fluid and the high-field spectral line clearly exhibits a signal from the paramagnetic probe in both lipid and the aqueous phases. The hyperfine splitting for the probe in the lipid phase of the DOPC-water system is the same as in the DMPC-water system: approximately 16.05 Gauss. Both at -60 C and at -2 C the spectra show no evidence of the existence of a liquid aqueous phase.

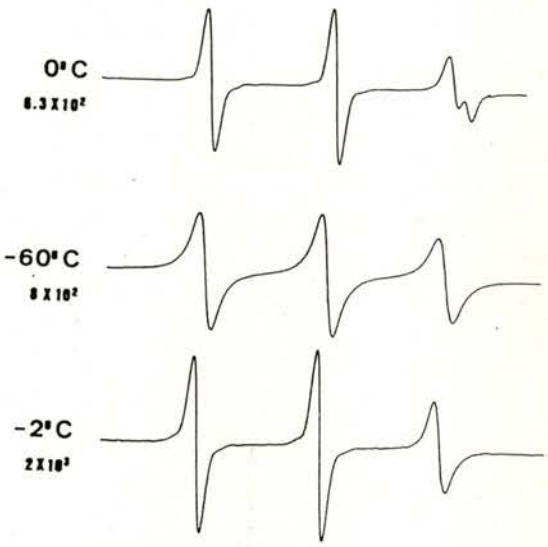

Figure 2 - ESR spectra of the nitroxide spin probe Tempo in DOPC-water systems at the indicated temperatures and gains.

The viscosity of the liquid aqueous phase, when present at -2 C (as is the case for the DMPC-water system), is greater than the viscosity of water at 0 C; $t_{water}^{(0)} = 3.6*10^{-12}$s while $t_{water}^{(-2)} = 7.5*10^{-11}$s. Similarly the viscosity of the lipid system increases as the temperature is lowered; while it is impossible to measure the viscosity of DMPC below its phase transition using these paramagnetic probes, because they are excluded from the lipid phase, the spectra in fig. 2 show that t_{lipid} increases from $4*10^{-10}$ s to $8.3*10^{-10}$ s as the temperature is lowered from -2 C to -60 C. Interestingly enough, it appears that once the water is frozen, lowering the temperature well below the freezing point of DOPC (i.e. below -20 C) increases the

viscosity of the lipid phase, but does not exclude the probe from the lipid environment. Such an observation is consistent with the idea that it is unlikely for the paramagnetic probe to be able to move in and out of the medium of frozen water; it is also consistent with our earlier observation that as the temperature is lowered below the transition temperature of DMPC (+23 C) the probe can be excluded from the lipid phase since it can now move into the liquid aqueous phase.

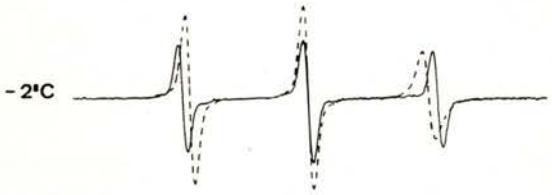

Figure 3 - Superimposed spectra of Tempo in DMPC (——) and DOPC-water (-------) systems at -2 C.

In Fig. 3 we have superimposed the spectra of Tempo in both the DMPC-water and the DOPC-water systems at -2 C; this figure leaves absolutely no doubt that at -2 C the only system that shows any fluid aqueous environment is the DMPC one. It could be argued that in the DOPC - water system at -2 C the solubility of the paramagnetic probe is much larger in the lipid environment than in this aqueous environment of "restricted" water (thereby explaining the absence of a probe signal from the latter environment); however additional experiments performed (data not shown) with other paramagnetic probes (Tempone and CAT_9), and at different concentrations, are in complete agreement with the results obtained with Tempo. Our results do not depend on the type or electrical charge of the paramagnetic probe used, and furthermore they show quite clearly that in lipid-water systems just below 0 C the presence or absence of a fluid aqueous environment depends on whether the lipid is already in the gel state or not. The nature (chemical structure) of this fluid (when compared to frozen water) aqueous environment, and its accurate quantification cannot be determined by our methodology; it seems, though, that our results indicate about 20-25 moles of water per mole of lipid, in agreement with other results [4]. It also appears that the term "restricted" might be appropriate when comparing it to fluid bulk water (above 0 C); in our case an equivalent amount of water remains fluid when compared to frozen bulk water (below 0 C) but only if the lipid is already in the gel state.

ACKNOWLEDGMENTS

This work was supported by the Instituto Nacional de Investigação Científica (INIC-Portugal).

REFERENCES

[1] Chapman, D., Williams, R.M. and Ladbrooke, B.D., Chem. Phys. Lipids **1**, 445 (1967).
[2] Elworthy, P.H., J. Chem. Soc., 5385 (1961).

[3] Finer, E. G. and Darke, A., Chem. Phys. Lipids **12**, 1 (1974).
[4] Salsbury, N. J., Darke, A. and Chapman, D., Chem. Phys. Lipids **8**, 142 (1972).
[5] Atkinson, D., Hanser, H., Shipley, G.G. and Stubbs, M., Biochem. Biophys. Acta **339**, 10 (1974).
[6] Keith, A.D., Snipes, W. and Chapman, D., Biochem. **16**, 634 (1977).
[7] Ladbrooke, B.D., Williams, R.M. and Chapman, D., Biochem. Biophys. Acta **150**, 333 (1968).
[8] Strauss, G. and Hauser, H., Proc. Natl. Acad. Sci. USA **83**, 2422 (1986).

EFFECTIVE ATOMIC NUMBERS OF TISSUE EQUIVALENT COMPOUNDS IN THE ENERGY REGION OF 1 TO 100 MeV FOR ELECTRONS AND IONS .

S. GURU PRASAD AND K. PARTHASARADHI*
Division of Medical Physics, Evanston Hospital, Northwestern University Medical School,
2560 Ridge Avenue, Evanston, Il 60201, U.S.A.

*Present Address:
Department of Nuclear Physics, Andhra University, Visakhapatman-530003
INDIA

ABSTRACT-A study of effective atomic numbers of tissue equivalent compounds has been carried out in the energy region 1 to 100 MeV for electrons and ions. It is noticed that in general the effective atomic number for electrons increases slightly with energy, for Helium ions remains more or less the same and for heavy ions it increases initially and then decreases.

1. INTRODUCTION

A systematic study of the interaction of photons, electrons and ions with biological materials and tissue equivalent compounds is important in the field of Radiation Physics. Accurate data about effective atomic numbers is required to evaluate the absorbed dose for the high energy beams produced by accelerators used in medicine. Reports on the attenuation coefficients and stopping powers of individual elements and a few compounds, mixtures and biological materials have appeared[1],[2]. White[4] performed a detailed study on the effective atomic numbers for photons and electrons for partial processes in biological materials. However, these studies are restricted to the Z exponents and their variation with energy. Investigations on effective atomic numbers and its variation with energy for partial as well as total interactions for photons are reported [4] in the energy region 10 to 200 KeV. On the basis of cross-section per electron, Yang et al[5] have derived effective atomic numbers which are less energy dependent in the low energy region. It appears that, in the high energy region, no study has been previously published on the total effective atomic numbers particularly for charged particles and ions. The present study is a comparison of the effective atomic numbers of tissue equivalent materials such as polyethylene, polystyrene, Nylon, Lexon, Plexiglass and Bakelite in the energy region 1 to 100 MeV for electrons and ions.

2. EVALUATIONS

The effective atomic numbers for photons of composite materials can be computed from the cross-section data of the con-

stituent elements according to the previous suggested procedures [5]. The mass attenuation coefficient of the composite material is the arithmetic sum of the mass attenuation coefficients of the constituent elements in the proportions they exist in the composite material (additivity law). The effective atomic number of the composite material can be directly extracted from a plot of the attenuation coefficient (expressed per atom) as a function of atomic number. Similarly, the effective numbers for the tissue equivalent materials are obtained by using the same procedures by substituting the stopping powers of electrons and ions in the place of attenuation coefficients. The proportions of the constituent elements of the materials are obtained from their chemical formulae. Mass stopping powers of the composite materials are tabulated in Table 1 and the derived effective atomic numbers are listed in Table 2. The error in the derived effective atomic numbers from the plots is of the order of 0.2.

3. DISCUSSION

It can be seen from Table 2 that, in general, the effective atomic numbers for the electrons increases slightly with the energy, for Helium ions it remains more or less the same and for Carbon and Neon ions it increases initially and then decreases. The effective atomic number at a particular energy depends on the relative dominations of the individual partial processes and their dependence on Z. The collisional and radiative processes are predominant for electrons. The relative contribution of the radiative process increases with the energy and has a higher Z dependence than the collisional process. Hence the effective atomic number for electrons increases with energy. Collisional loss is the dominant interaction for ions in the present energy region. Consequently, the effective atomic number for He ions remains more or less the same. However, in the case of C and Ne ions, the observed trends may be due to charge exchange effects.

In the present study the chemical effects due to elemental bonding are neglected by the application of additivity law. This effect is not well understood for ions and is not expected to be higher at higher energies [2]. The usual way for accounting for chemical effect for electrons is to use the mean excitation energy of the compound computed theoretically. The effective atomic numbers are evaluated for four materials from the available data [1],[2] and are listed in Table 3. It is seen that the chemical bonding on the effective atomic number is not very significant in those materials within the range of errors.

REFERENCES

[1] ICRU Reports 35, and 37, Stopping Powers for Electrons and Positrons, 1984.

[2] Northcliffe, L.C. and Schlling, R.F., Range and Stopping Power Tables for Heavy Ions, Nuclear Data Tables **A7**, 233-292, 1970.

[3] Thirumala Rao, B.V., Raju, M. L. N., Narasimham, K.L., Parthasaradhi, K. and Mallikarjuna Rao, B., Interaction of low energy photons with biological materials and the Effec-

tive Atomic Numbers, Medical Physics **12**, 745-748, 1985.

[4] White, D.R., Analysis of the Z-dependence of the Photon and Electron Interactions, Physics in Medicine and Biology, **22**, 219-228, 1971.

[5] Yang, N.C., Leichner, P.K. and Hawkins, W.G., Effective Atomic Numbers for the low Energy Photon interactions in human tissues, Medical Physics, **14**, 759-766, 1987.

TABLE 1

MASS STOPPING POWERS

ELECTRONS (MeV cm^2/gm)

	Energy in MeV					
	1	5	10	20	50	100
Polyethylene	1.936	2.071	2.255	2.536	3.245	4.345
Polystyrene	1.790	1.911	2.082	2.353	3.056	4.174
Nylon	1.849	2.010	2.210	2.517	3.285	4.465
Lexan	1.749	1.892	2.078	2.371	3.124	4.308
Plexiglass	1.810	1.967	2.180	2.495	3.286	4.505
Bakelite	1.753	1.893	2.077	2.368	3.115	4.292

C IONS (MeV cm^2/gm)

	Energy in MeV					
	0.96	4.80	9.60	19.20	48.00	96.00
Polyethylene	6.415	11.166	9.671	6.833	3.649	2.128
Polystyrene	5.897	9.671	8.413	6.023	3.327	1.954
Nylon	5.602	10.097	8.729	6.195	3.394	1.990
Lexan	5.393	5.393	7.916	5.679	3.186	1.879
Plexiglass	5.358	9.637	8.336	5.934	3.285	1.932
Bakelite	5.444	9.165	7.961	5.711	3.119	1.886

He IONS (MeV cm^2/gm)

	Energy in MeV				
	1.007	5.008	10.007	20.013	48.031
Polyethylene	2.684	1.138	0.618	0.347	0.173
Polystyrene	2.368	0.555	0.317	0.159	0.996
Nylon:	2.408	1.025	0.568	0.324	0.162
Lexan:	2.216	0.935	0.527	0.305	0.153
Plexiglass:	2.303	0.979	0.547	0.313	0.158
Bakelite:	2.230	0.941	0.530	0.306	0.154

Ne IONS (MeV cm^2/gm)

	Energy in MeV					
	0.996	4.998	9.996	19.992	49.980	99.960
Polyethylene:	7.101	18.280	22.012	18.673	11.708	7.733
Polystyrene:	6.549	16.129	18.974	16.259	10.515	7.076
Nylon:	6.187	16.401	19.911	16.764	10.767	7.210
Lexan:	5.977	15.096	17.898	15.229	9.998	6.789
Plexiglass:	5.917	15.687	18.998	15.982	10.336	6.989
Bakelite:	6.036	15.193	17.993	15.324	10.046	6.815

TABLE 2

EFFECTIVE ATOMIC NUMBERS

		Energy in MeV*					
		1	5	10	20	50	100
Polyethylene	e	2.6	2.5	2.5	2.6	2.8	3.1
	He	3.0	2.7	2.5	2.6	2.7	-
	C	2.8	3.0	2.8	2.6	2.5	2.5
	Ne	2.8	3.1	3.0	2.7	2.5	2.6
Polystyrene	e	3.5	3.5	3.6	3.6	3.8	4.0
	He	3.7	3.6	3.3	3.4	3.5	-
	C	3.2	3.8	3.8	3.5	3.4	3.4
	Ne	3.1	3.7	4.0	3.7	3.3	3.4
Nylon	e	3.3	3.3	3.3	3.5	3.6	4.0
	He	3.4	3.2	3.1	3.1	3.2	-
	C	3.0	3.7	4.1	3.2	3.1	3.2
	Ne	2.9	3.5	3.8	3.3	3.2	3.1
Lexan	e	4.2	4.2	4.3	4.4	4.5	4.6
	He	4.0	4.1	3.9	3.9	4.0	-
	C	3.4	4.3	5.0	4.0	3.9	4.0
	Ne	3.2	4.0	4.6	4.2	3.9	3.9
Plexiglass	e	3.6	3.7	3.8	4.0	4.2	4.3
	He	3.7	3.6	3.4	3.4	3.5	-
	C	3.1	3.8	4.0	3.6	3.4	3.5
	Ne	3.0	3.7	4.2	3.2	3.4	3.5
Bakelite:	e	4.0	4.1	4.2	4.4	4.5	4.6
	He	4.0	4.1	3.8	3.9	4.0	-
	C	3.4	4.3	4.9	3.9	3.9	3.9
	Ne	3.2	3.9	4.8	4.2	3.9	3.9

*The ion energies are very close to the energies mentioned.

TABLE 3

EFFECTIVE ATOMIC NUMBERS FOR ELECTRONS

		Energy in MeV					
		1	5	10	20	50	100
Nylon	w/o	3.3	3.3	3.3	3.5	3.6	4.0
	wc	3.2	3.2	3.1	3.3	3.4	4.7
Lexan	w/o	4.2	4.2	4.3	4.4	4.5	4.6
	wc	4.1	4.1	4.1	4.2	4.4	4.5
Polyethylene	w/o	2.6	2.5	2.6	2.6	2.8	3.1
	wc	2.6	2.5	2.5	2.5	2.7	2.9
Polystyrene	w/o	3.5	3.5	3.6	3.6	3.8	4.0
	wc	3.5	3.5	3.5	3.6	3.7	3.9

w/o - without chemical effect
wc - with chemical effect

THE USE OF LINEAR INVERSE TECHNIQUES IN GEOTHERMAL STUDIES

ANTÓNIO CORREIA
Departamento de Física Universidade de Évora
7000 Evora, Portugal
and
Department of Physics University of Alberta
Edmonton, Alberta, Canada T6G 2J1

ABSTRACT-The knowledge of the present day temperature distribution within a basin is important both as a constraint for thermal evolution models, and as an indication of the processes that may have governed the thermal state of the basin through time. These aspects are essential for the complete understanding of gas and oil maturation in sedimentary basins. In this paper, general ideas about inversion and an inversion method to estimate geothermal gradients from bottom-hole temperature measurements are presented. Combining the gradients with thermal conductivity information makes it possible to estimate the heat flow density that constitutes the most important thermal parameter in geothermal studies. Bottom-hole temperature measurements are generally abundant in sedimentary basins because of the high number of wells drilled for gas and oil exploration. However, they are of poor quality and in this case inversion methods have given better results than the traditional ones.

1.INTRODUCTION

In spite of the fact that the distribution of temperature inside the Earth is probably one of the most fundamental parameters needed to understand its evolution and behaviour, it remains one of the most poorly determined Earth properties. Knowledge and evaluation of the internal temperature of the Earth is obtained through measurements of geothermal gradients in wells or, equivalently, through the calculation of heat flow density (HFD) near the surface. Unfortunately, reliable geothermal gradient measurements are relatively rare due to well drilling costs and scarcity of appropriate wells. Besides, since the temperature distribution within the Earth is a continuous function and the surface measurements are discrete, the problem of its interpretation is never unique.

The problem of trying to determine the temperature distribution at a given depth is further complicated by the fact that there are uncertainties in the radiogenic heat production of rock formations and, at the same time, the heat transfer mode is generally very complicated, i.e., non steady-state conduction and convection of heat by fluid motion. Measurements of HFD at the Earth's surface provide, however, constraints on its internal temperature distribution and therefore many heat flow density studies are being performed.

Because of hydrocarbon exploration, sedimentary basins provide a great amount of temperature data that can be used to determine, analyze and interpret the temperature distribution within the Earth. These data exist in the form of bottom-hole temperatures (BHT) and, despite their quantity, their quality is generally low. Nevertheless, because of the large numbers of BHTs available for analysis, statistically significant information is contained in these data sets [2], [9],[10],[15],[18].

Several methods have been proposed to analyze BHTs measured in oil wells. There are essentially two ways of approaching this problem. In the first one [2], [7], [8], [9], [16], the calculation of geothermal gradients or heat flow density is considered a forward problem, while in the second one [10], [18], [19], it is considered a linear discrete inverse problem.

Inverse theory was developed by scientists and mathematicians who had different backgrounds and goals and, therefore, the resulting versions look different, in spite of the fact that they are fundamentally similar. There are three major approaches to inverse theory [17]. The first is based on probability theory. In this version the data (measured values) and the model parameters (estimated values) are treated as random variables and the emphasis is placed on the determination of their probability distributions. The second, developed from more deterministic physical sciences, emphasizes the estimation of model parameters and associated errors rather than probabilistic distributions. The third approach was developed from the consideration that model parameters are intrinsically continuous functions rather than discrete, as considered in the two first approaches.

In this work only the Gaussian linear discrete inverse theory will be considered. A review of some of the linear inverse techniques will be presented as well as the way to apply them to the study of the temperature distribution inside the Earth using bottom-hole temperatures obtained in oil wells.

2.GENERAL IDEAS AND DESCRIPTION OF DISCRETE INVERSE PROBLEMS

Inverse theory consists of a set of mathematical techniques for reducing data to obtain information about the physical world. The inferences and numerical or statistical values obtained through the use of inverse theory, which are generally called "model parameters", are based on observations or simply "data". Of course, some relationship must exist between the data and the model parameters, usually a mathematical theory or model. Generally speaking, the phrase "inverse theory" is used in contrast to "forward theory". The latter is defined as the process of determining the results of measurements or data based on some specific model. The former is defined as the process of estimating the model parameters from a tabulation of measurements or data and a specific model. It is worthwhile to note that inverse methods do not provide any information about the model itself. However, in some cases they can give some

insight on the correctness of a given model or a way of discriminating between several possible models.

In most inverse problems the data are a sequence of numerical values (**d**) and therefore vectors constitute a convenient means to represent them. The same applies to the model parameters (**m**). These two quantities are generally related by one or more implicit equations such as

$$\begin{aligned} f_1(\mathbf{d},\mathbf{m}) &= 0 \\ f_2(\mathbf{d},\mathbf{m}) &= 0 \\ &\cdot \\ &\cdot \\ &\cdot \\ f_L(\mathbf{d},\mathbf{m}) &= 0 \end{aligned} \qquad (1)$$

where L is the number of equations. These equations can be compactly written as a vector equation

$$\mathbf{f}(\mathbf{d},\mathbf{m}) = 0 \qquad (2)$$

which summarizes what is known about how the data and the unknown model parameters are related. The main purpose of the inverse theory is to solve these equations for the model parameters. In general, the system of equations (1) consists of arbitrarily non-linear functions of the data and model parameters. Also, in most cases, it does not contain enough information to uniquely determine the model parameters. There are, however, many problems where the system of equations (1) takes one of several simple forms. If **f** is linear in both data and model parameters, equation (2) can be written as a matrix equation

$$\mathbf{f}(\mathbf{d},\mathbf{m}) = 0 = \mathbf{F}\begin{bmatrix}\mathbf{d}\\ \mathbf{m}\end{bmatrix} \qquad (3)$$

where **F** is a L*(M+N) matrix, M is the number of elements of the model parameter matrix, and N is the number of elements of the data matrix. If it is possible to separate the data from the model parameters and to form L=N equations that are linear in the data and non-linear in the model parameters, then equation (2) can be written as

$$\mathbf{f}(\mathbf{d},\mathbf{m}) = 0 = \mathbf{d} - \mathbf{g}(\mathbf{m}) \qquad (4)$$

where **g**(**m**) represents a non-linear function of the model parameters. If in equation (4) **g** is also linear, equation (2) can be written as

$$\mathbf{f}(\mathbf{d},\mathbf{m}) = 0 = \mathbf{d} - \mathbf{G}\mathbf{m} \qquad (5)$$

where **G** is a N*M matrix.

Equation (5) corresponds to the simplest and best understood inverse problems and constitutes the foundation of the study of discrete inverse theory. Fortunately, this equation appears in many physical science problems, and even some non-linear problems can be reduced to it in certain cases. Matrix **G** is called the data kernel in analogy with continuous inverse theory where the function $G(x,\xi)$ is the kernel of an integral equation [3], [4], [5] .

The simplest solution to an inverse problem is an estimate of the model parameters, $\mathbf{m}^{est}$. This consists on a numerical sequence of values, which in certain

cases can be misleading. In fact, estimates in themselves do not give any information about the quality of the solutions and therefore there is no control of the errors in the model parameters estimation. One way to partially solve the problem is to define either absolute or probabilistic bounds that allow an assessment of the degree of certainty of the solution. Absolute bounds imply that the true value of a given model parameter lies between two stated values, which is equivalent asserting an absolute error to the estimate. Probabilistic bounds imply that the estimate is likely to be between the bounds with some degree of certainty; a generalization of this consists in stating the complete probability distribution for the model parameters.

There are three points of view that can be used to study Gaussian linear inverse problems [1], [17]. The first point of view [11] that is generally called the length or stochastic method, emphasizes the data and the model parameters themselves, and the method of least squares is used to estimate the model parameters with the smallest prediction error. This approach will be detailed in the next section since it seems to be the most suitable one to apply to geothermal problems. The second point of view [13] emphasizes the relationship between the data and the model parameters. It is called the method of generalized inverses and it provides a means to tell a well designed experiment from a poor one, even without knowing the numerical values of the data and model parameters. The third point of view is called the method of maximum likelihood and it assumes that the optimum values of the model parameters maximize the probability that the observed data are in fact observed. This third point of view will not be described in this work.

Before describing in a more formal way the stochastic inversion point of view it is useful to define the concepts of underdetermined, even-determined, and overdetermined inverse problems, and *a priori* information.

Linear inverse problems are said to be underdetermined when equation (5) does not provide enough information to uniquely determine all the model parameters or, in a simpler manner, when there are more unknown model parameters than data. This case generally happens when there are several solutions to the problem that have zero prediction error (by definition the prediction error is given by $e_i = d_i^{obs} - d_i^{pre}$, where d_i^{obs} is the measured data and d_i^{pre} is the predicted data obtained using the estimated model parameters).

Even-determined problems appear when there is just enough information to determine the model parameters. In this case there is only one solution to the problem and the prediction error is zero.

Overdetermined problems happen when there is too much information contained in equation (5). In this case there are several solutions and the method of least squares is used to obtain the best approximate solution. Overdetermined problems have typically more data than unknown model parameters.

To obtain a solution to an inverse problem it is necessary to choose one solution from the great number of solutions generally available. This is particularly true in the underestimated problem. To achieve that, information that is not contained in equation (5) must be given. This extra information is called *a priori* information [12] and generally quantifies expectations about the character of the solution that are not based on the actual data.

3. THE LENGTH OR STOCHASTIC INVERSION METHOD

In this method the main idea is to determine the model parameters so that the predicted data are as close as possible to the observed data. The predicted data are calculated using the estimated model parameters and, therefore, for each observation it is possible to define the above-mentioned prediction error, e_i. The best solution will then be that which makes the overall error E, defined as

$$E = \sum_{i=1}^{N} e_i^2 \qquad (6)$$

a minimum. In vector terms this can be written

$$E = \mathbf{e}^T \mathbf{e} \qquad (7)$$

where T means transpose and $\mathbf{e}$ is the vector column formed by the values of e_i. Using the least squares method it is then possible to find the model parameters that minimize a particular measure of the length of the estimated data, $\mathbf{d}^{est}$, from the observations, $\mathbf{d}^{obs}$.

The term norm is generally used to refer to some measure of length and is indicated by a set of vertical bars. Several norms can be used but the most common is the L_2 norm defined as

$$\|\mathbf{e}\|_2 = \left(\sum_i |e_i|^2 \right)^{\frac{1}{2}}. \qquad (8)$$

This norm is used in the method of least squares to quantify length and implies that the data obey Gaussian statistics [17]. Using equation (7), it is possible to calculate the least squares solution to the linear inverse problem defined by equation (5):

$$E = \mathbf{e}^T\mathbf{e} = (\mathbf{d} - \mathbf{Gm})^T(\mathbf{d} - \mathbf{Gm}) = \sum_i^N \left(d_i - \sum_j^M G_{ij} m_j \right) \left(d_i - \sum_k^M G_{ik} m_k \right) \qquad (9)$$

Multiplying and reversing the order of the summations leads to

$$E = \sum_j^M \sum_k^M m_j m_k \sum_i^M G_{ij} G_{ik} - 2 \sum_j^M m_j \sum_i^N G_{ij} d_i + \sum_i^N d_i d_i \qquad (10)$$

The derivatives $\partial E / \partial m_q$ should now be computed. Performing this differentiation term by term gives for the first term

$$\frac{\partial}{\partial m_q} \left(\sum_j^M \sum_k^M m_j m_k \sum_i^N G_{ij} G_{ik} \right) =$$

$$\sum_j^M \sum_k^M [\delta_{jq} m_k + m_j \delta_{kq}] \sum_i^N G_{ij} G_{ik} = 2 \sum_k^M m_k \sum_i^N G_{iq} G_{ik} \qquad (11)$$

The second term gives

$$-2 \frac{\partial}{\partial m_q} \left(\sum_j^M m_j \sum_i^N G_{ij} d_i \right) = -2 \sum_j^M \delta_{jq} \sum_i^N G_{ij} d_i = -2 \sum_i^N G_{iq} d_i \qquad (12)$$

The third term is of course zero because

$$\frac{\partial}{\partial m_q} \left(\sum_i^N d_i d_i \right) = 0 \ . \qquad (13)$$

Combining equations (11), (12) and (13) gives

$$\partial E / \partial m_q = 0 = 2 \sum_k^M m_k \sum_i^N G_{iq} G_{ik} - 2 \sum_i^N G_{iq} d_i \qquad (14)$$

which in matrix notation can be written as

$$\mathbf{G^T G m} - \mathbf{G^T d} = 0 \ . \qquad (15)$$

Assuming that $[\mathbf{G^T G}]^{-1}$ exists, the solution for the model parameters estimate is

$$\mathbf{m}^{est} = [\mathbf{G^T G}]^{-1} \mathbf{G^T d}. \qquad (16)$$

When dealing with an inverse problem the question that always arises is if there is a solution to it and, in the affirmative case, if the solution is exact.Equation (16) implicitly assumes that there is only one "best" solution. However, it can be proved that least squares fails if the number of solutions that give the same minimum prediction error is greater than one [17]. That is the case, for instance, when a straight line must be chosen to pass through only one data point. Of course, in this situation the solution is non-unique and many possible straight lines can pass through the data point, each solution presenting zero prediction error.

Data always contain noise that causes errors in the estimated model parameters. Since the formulas to determine the model parameters are linear functions of the data ($\mathbf{m}^{est} = \mathbf{Md} + \mathbf{v}$, where $\mathbf{M}$ is a matrix and $\mathbf{v}$ is a vector), it is possible to calculate how the measurement errors influence the errors in the estimated model parameters. If the data have a distribution characterized by some covariance matrix [cov **d**], the estimates of the model parameters have a distribution characterized by [cov **m**] = $\mathbf{M}$[cov **d**]$\mathbf{M}^T$ .If it is possible to assume that the data are uncorrelated and all of equal variance σ_d^2, simple formulas are obtained for the simple inverse problem solutions. The simpler least squares solution represented by equation (16) has covariance

$$[\text{cov } \mathbf{m}] = \sigma_d^2 [\mathbf{G^T G}]^{-1} \ . \qquad (17)$$

that shows that the covariance matrix of the model parameters depends on the variance of the data [17].

4.THE USE OF INVERSE THEORY IN HEAT FLOW STUDIES

When analyzing the thermal state in sedimentary basins, one of the limiting factors is the quantity and quality of the temperature data available. Accurate temperature measurements are rare. However, for most basins, a great amount of data exists in the form of bottom-hole temperatures (BHTs) obtained during geophysical logging operations. Unfortunately, the quality of the BHT measurements is low.

Numerous recent studies of basins have used BHTs for different types of geothermal analysis to try to find which gives the best results. One of the methods that has recently received attention is the linear inversion method which was first applied to the Michigan Basin [18]. In this method, the area under study is divided into m discrete layers that may be formations or lithologic units. Each of these layers is assumed to have constant thermal conductivity, K_j (j=1,2,...,m); heat flow density is assumed to be constant throughout the entire area. This implies that the geothermal gradients, g_j , are constant in each layer or formation. Using the thermal resistance method proposed in reference [6], the temperature at any depth can be obtained by

$$T = T_0 + q \sum_j (z_j / k_j) \qquad (18)$$

where T_0 is the temperature at the surface of the Earth, q is the heat flow density, z_j is the thickness of the jth layer, and K_j is the thermal conductivity of the same layer. After correcting BHTs by one of the available methods (the Horner plot technique, for instance [14]), equation (18) can be modified to:

$$(BHT - T_0)_i = \Delta T_i = \sum_j z_{ij} g_j \qquad (19)$$

where z_{ij} is the thickness of the jth formation at the ith well. If the number of BHTs, n, is greater than the number of unknown formation geothermal gradients, m, an overdetermined system of n equations in m unknowns exists and the BHT data can be inverted for the geothermal gradients, g_j , in each formation. These estimated gradients may then be used in a forward sense to calculate the best temperature field or, combined with thermal conductivity data, to estimate the heat flow density.

In what follows, the variables that are generally used in heat flow density studies will be substituted into the equations described in the previous paragraph.

To apply inverse theory to geothermal studies two assumptions are usually made: first, heat transfer only occurs in the vertical direction and is purely conductive; second, the average geothermal gradients are constant over each formation. Given these assumptions, equation (19) can be written in matrix form as

$$\underset{\sim}{T}_{\Delta} = \underset{\approx}{Z}\,\underset{\sim}{g} \qquad (20)$$

where $\underset{\sim}{T}_\Delta$ is the vector of n temperature differences, $\underset{\approx}{Z}$ is a (n*m) matrix of formation thicknesses, and g is the vector of m unknown geothermal formation gradients. Because $\underset{\sim}{T}_\Delta$ contains noise, and the model generally used is only an approximation to physical reality, it is unlikely that an exact solution exists. The inverse problem then becomes one of finding a set of formation gradients that minimizes the error

$$\underset{\sim}{r} = \underset{\sim}{T}_\Delta - \underset{\approx}{Z}\,\underset{\sim}{g}_{est} \qquad (21)$$

where g_{est} is the best estimate of the true formation gradient. Therefore, for the ith well there is a residual, r_i, given by

$$r_i = \Delta T_i - \sum_{j=1}^{m} z_{ij}\, g_{est\,j} \qquad (22)$$

where ΔT_i is the measured temperature difference, and the second term on the right hand side of the equation is the estimated temperature difference calculated using the inverse solution. Applying the least squares approach, the solution will be the one that makes the sum of the squares of the residuals, r_i, a minimum. In terms of the variables common to heat flow studies, equation (16) takes the form

$$\underset{\sim}{g}_{est} = \left(\underset{\approx}{Z}^T \underset{\approx}{Z}\right)^{-1} \underset{\approx}{Z}^T \underset{\sim}{T}_\Delta \ . \qquad (23)$$

Since this equation does not preclude negative geothermal gradients as solutions and they are geologically unreasonable, the solution must be constrained to be non-negative. This condition constitutes *a priori* information.

The variance σ_d^2 of the temperature is estimated by

$$\sigma_d^2 = \sum_{i=1}^{n} r_i^2 / (n - m) \qquad (24)$$

and the variance σ_m^2 of the jth estimated geothermal gradient is the jth diagonal element of the covariance matrix [10]

$$\sigma_m^2 = \sigma_d^2 \left(\underset{\approx}{Z}^T \underset{\approx}{Z}\right)^{-1}_{jj} \ . \qquad (25)$$

5. CONCLUSIONS

Compared to other methods for processing BHT data sets, the linear inverse method described in the previous paragraphs has several advantages. An easy linear solution is generally obtained and the theory provides methods to deal with data error. Furthermore, insufficient data and non-uniqueness of the solution are explicitly dealt with. It also allows all the available data to be included in the calculation, specifying how data of different quality should be weighted. Finally, it provides the means to estimate the variance of the error in each model parameter, giving a relative and absolute measure of the quality of the solution [19].

In the length point of view of the Gaussian linear inverse problem, the data and model parameters are treated as random variables and it is assumed that they have a certain probability distribution, which

in fact constitutes *a priori* information. The inverse methodology then returns the minimum variance solution, that is, the solution that best fits within the probable ranges of the data and model parameters and minimizes the variance of the error in that solution.

ACKNOWLEDGEMENTS

This review was originally suggested by Dr. E. Kanasewich, who also gave suggestions which greatly improved the first draft of the manuscript. Dr. M. Victor and Dr. F. W. Jones are also thanked for their constructive comments and revision of the paper. This review was prepared while the author was at the Department of Physics of the University of Alberta, Canada, under a leave of absence from the Physics Department of the University of Évora, Portugal. The author received financial support by the University of Évora, the Junta Nacional de Investigação Científica e Tecnológica, Portugal, and the University of Alberta through a teacher assistantship.

REFERENCES

[1] Aki, K. and Richards, P. G., Quantitative Seismology, Theory and Methods, **II**, W. H. Freeman and Co. (1980).

[2] Andrews-Speed, C. P., Oxburgh, E. R., and Cooper, B. A. , Temperatures and depth--dependent heat flow in Western North Sea, Am. Assn. Petr. Geol. Bull., **68**, 1764-1781 (1984).

[3] Backus, G. E., and Gilbert, J. F., Numerical application of a formalism for geophysical inverse problems, Geophys. J. R. Astron. Soc., **13**, 247-276 (1967).

[4] Backus, G. E., and Gilbert, J. F., The resolving power of gross Earth data, Geophys. J. R. Astron. Soc., **16**, 169-205 (1968).

[5] Backus, G. E., and Gilbert, J. F., Uniqueness in the inversion of gross Earth data, Phil. Trans. Roy. Soc. London, Ser. **A 266**, 123-192 (1970).

[6] Bullard, E. C., Heat flow in South Africa, Proc. R. Soc. London, Ser. **A. 173**, 474-502 (1939).

[7] Carvalho, H. D. S., and Vacquier, V., Method for determining terretrial heat flow in oil fields, Geophysics, **42**, 584-593 (1977).

[8] Carvalho, H. D. S., Purwoko, Siswoyo, Thamrin, M., and Vacquier, V., Terrestrial heat flow in the Tertiary Basin of Central Sumatra, Tectonophysics, **69**, 163-188 (1980).

[9] Chapman, D. S., Keho, T. H., Bauer, M. S., and Picard, M. D., Heat flow in the Uinta Basin determined from bottom hole temperature (BHT) data, Geophysics, **49**, 453-466 (1984).

[10] Deming, D., and Chapman, D. S., Inversion of bottom-hole temperature data: the Pineview field, Utah-Wyoming thrust belt, Geophysics, **53**, 707-720 (1988).

[11] Franklin, J. N., Well-posed stochastic extensions of ill-posed linear problems, J. Math. Anal. and Appl., **31**, 682-716 (1970).

[12] Jackson, D. D., The use of *a priori* data to resolve non-uniqueness in linear inversion, Geophys. J. Roy. Astron. Soc., **57**, 137-157 (1979).

[13] Kanasewich, E. R., Time sequence analysis in Geophysics, The University of Alberta Press (1985).

[14] Lachenbruch, A. H., Brewer, M. C., Dissipation of the temperature effect of drilling a well in Artic Alaska, U.S. Geol. Surv. **1083C**, 73-109 (1959).

[15] Lam, H. L., and Jones, F. W., A statistical analysis of bottom-hole temperature data in the Hinton area of West-Central Alberta, Tectonophysics, **103**, 273-281 (1984).

[16] Majorowicz, J. A., Jones, F. W., Lam, H. L., and Jessop, A. M., The variability of heat flow both regional and with depth in Southern

Alberta, Canada: effect of ground water?, Tectonophysics, **106**, 1--29 (1984).
[17] Menke, W., Geophysical data analysis: discrete inverse theory, Academic Press Inc. (1984).
[18] Speece, M. A., Bowen,T. D., Folcik, J. L., and Pollack, H. N., Analysis of temperatures in sedimentary basins: the Michigan Basin, Geophysics, **50**, 1318-1334 (1985).
[19] Willett, S. D., and Chapman, D. S., Analysis and interpretation of temperatures and thermal processes in the Uinta Basin, in Beaumont, C., and Tankard, A. J., Sedimentary basins and basin-forming mechanisms, Can. Soc. Petr. Geol., Memoir **12**, 447-461 (1987).

ROLE OF CARBON INCORPORATION ON STRUCTURAL AND TRANSPORT PROPERTIES OF a/μc-Si:C:H FILMS

M. VIEIRA, R. MARTINS, E. FORTUNATO, M. SANTOS, A. MAÇARICO, N. CARVALHO AND L. GUIMARÃES

Faculdade de Ciências e Tecnologia da Universidade Nova de Lisboa/ UNINOVA/ INIC
Quinta da Torre, 2825 Monte da Caparica, Portugal

ABSTRACT-Undoped and doped hydrogenated amorphous/microcrystalline silicon-carbon films (a/μc-Si:C:H) have been produced by the decomposition of silane-methane mixtures (SiH_4+CH_4), in a Two Consecutive Decomposition Deposition Chamber (TCDDC) system, assisted by electromagnetic static fields. The fraction, x, of CH_4 in the gas phase was determined as being $x=(CH_4)/(SiH_4+CH_4)$ and was varied in the range of 0.1 - 0.8. Through RBS (Rutherford Back Scattering), IR (Infra-Red), dark conductivity, σ_d, and optical absorption methods, it was observed that as carbon concentration, C_C, increases, the hydrogen content, C_H, decreases, leading to different structural and electro-optical properties of the films. This can be explained not only by an increase of CH_4 in the gas phase, but also by the power density, dp, used. For dp <10 $mWcm^{-3}$, the direct rate of CH_4 decomposition is very small and so CH_4 works as a "buffer gas". If the applied power is high enough (dp > 80 $mWcm^{-3}$) to decompose the CH_4, the species formed will be incorporated in the growing surface, mainly in tetrahedral bonds. By using mixtures heavily doped (with PH_3 and B_2H_6) and highly diluted in H_2, it is possible to produce μc-films highly conductive and weakly absorbing. Results concerning optical gap, E_{op},σ_d and activation energy, ΔE, recorded on these films will be also reported.

1-INTRODUCTION

Amorphous silicon carbide films have been extensively studied due to the possibility of achieving valence controllability over a wide range, either by change gas phase mixtures or by doping. This makes such alloys quite attractive to be used as "window layers" in solar cells since they present a low absorption in the visible range. Besides this, as they present large range Eop, by producing p[n](Si:C(B).i.n[p] heterojunctions, the open circuit voltage, V_{OC}, of such devices is enhanced.

Nevertheless, the results obtained up to now show that a-Si:C:H films have a low σ_d ascribed to a high ΔE, which is a limitation for improving further V_{OC} or the current collected [1].

Last year, Hamakawa et al.[2] proved to be possible to produce μc-Si:C:H films by ECR method [3]. Such layers when used in p[n](Si:C(B).i.n[p] heterojunctions structures lead to devices with better performances than the normal ones

(specially, V_{OC} and the short circuit intensity, are enhanced).

Another field of application of amorphous silicon-carbide films concerns their use as "buffer layers" in order to stop interdiffusion between ad-layers [4] and in producing superlattices based on a-Si/a-$Si_{1-x}:C_x$:H structures [5].

In this paper we shall report results concerning to a/μc-Si:C:H films produced by a TCDDC system [6] with electro-optical and structural properties that make them suitable to be used on several optoelectronic devices such as solar cells and TFT's, either as doped layers (μc-films) or blocking layers (a-films).

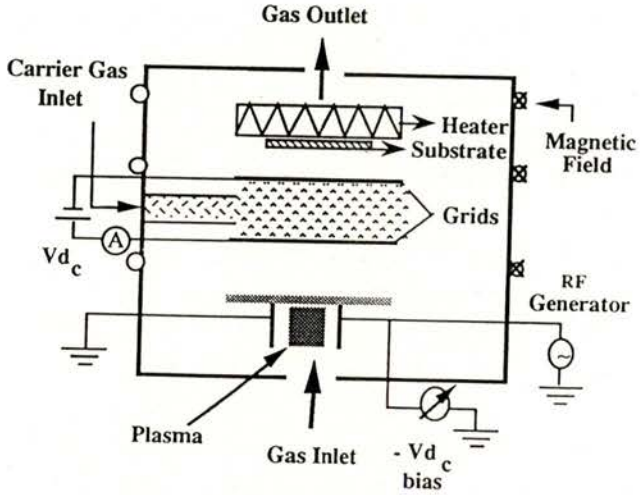

Fig. 1 - Sketch of the TCDDC system used

2-EXPERIMENTAL RESULTS

Films under analysis were produced by a TCDDC system in the presence of electromagnetic static fields as we show in Fig.1. Typical deposition conditions such as temperature, deposition pressure, gas flow rate and dp are shown in Table 1.

Electro-optical properties, microstructure, morphology and chemical composition have been analyzed using the apparatus and sample arrangements as described elsewhere [6]. The electro-optical properties have been deduced from dark conductivity and absorbance measurements. The correlation between, σ_d and E_{op} (inferred from Tauc's plot) with x, is presented in Fig. 2 for different dp [Fig. 2a), dp = 4 $mWcm^{-3}$; Fig. 2b), dp = 140 $mWcm^{-3}$], for alloys lightly doped with boron (B_2H_6/SiH_4 = 50 ppm).

In Fig. 3, we show the change in bond configurations of the IR spectra (between 900 cm^{-1} and 500 cm^{-1}), either for films produced at the same dp or alloy composition, with the same doping level. The dependence of C_H (inferred from IR

TABLE 1 - Typical deposition parameters

Gases	Gas flow (sccm)	Pressure (torr)	Temp. (C)	dp ($mWcm^{-3}$)
SiH_4	1 - 15			
CH_4	1 - 15	0.1 - 0.5	100 - 300	3 - 150
B_2H_6 / H_2	1 - 2			
H_2	50 - 400			

wagging modes [7]) and C_C (taken from RBS measurements) on x, for dp>60 $mWcm^{-3}$ is also shown in Fig. 4, for amorphous films.

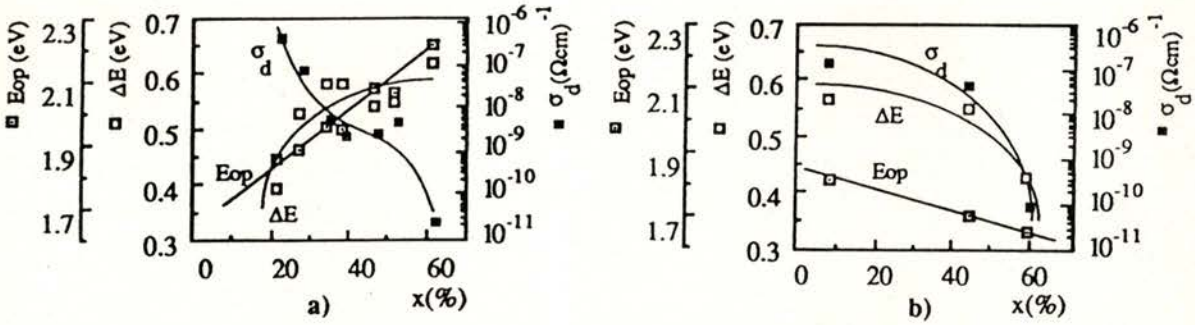

Fig. 2 -- E_{op}, ΔE and σ_d as a function of x : a) dp = 4 $mWcm^{-3}$; b) dp = 140 $mWcm^{-3}$

By using mixtures highly diluted in H_2 (SiH_4/H_2<3%) and doping levels higher than 1%, microcrystalline films are obtained if dp>80$mWcm^{-3}$.

In Fig. 5 we show a cross-section from a transmission electrophotograph of a n-type μc-$Si_{1-x}:C_x$:H film showing Si crystallites of the order of 100 angstrom embedded in an amorphous matrix. In Fig. 6 we show the results concerning ESCA measurements performed on n-type μc-films, while in Fig. 7 we show the dependence of σ_d and ΔE on E_{op} for p- and n-type μc-films.

3-ANALYSIS OF THE RESULTS AND COMMENTS

a) Optoelectronic properties:

The correlation between σ_d, ΔE and E_{op} on x is shown in Fig. 2 for different dp levels. The results show a transition on film's behaviour when x = 0.5. The obtained data show that:

i)*At low dp*

-When x <0.5 and dp = 4 mWcm^{-3} we observe a sharp decrease on σ_d, while ΔE and E_{op} increase on carbon incorporation,

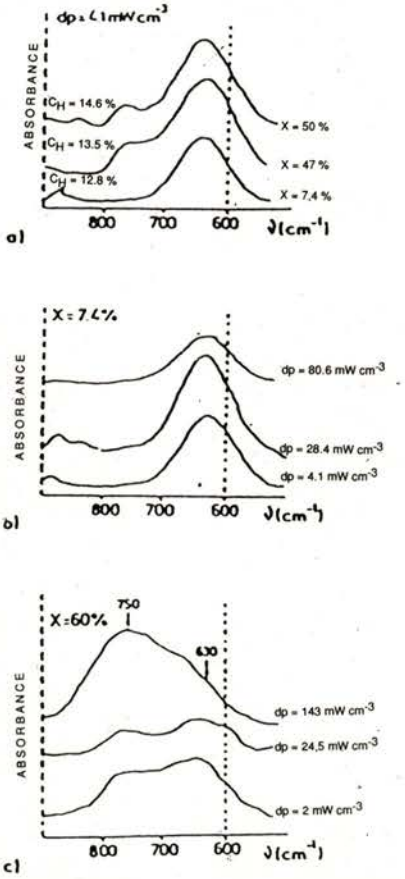

Fig.3 - IR spectra of a/μc-Si:C:H at: a)dp=4mWcm^{-3}; b) x=7% and dp variable; c) x=60% and dp variable.

mainly as -CH_3 (methyl) radicals (the rate of direct decomposition of CH_4 is very small).

-When x >0.5 although σ_d still decreases and E_{op} increases, ΔE tends to saturate as x increases. This can be explained by an enhancement of the methyl species incorporated.

ii)*At high dp*

-When x <0.5 and dp = 140 mWcm^{-3} we observe that E_{op} decreases slowly with x, while σ_d and ΔE are kept almost constant. This can be ascribed to a change in the way in which carbon is incorporated in the amorphous matrix. Now, there is an enhancement of the ionic bombardment on the growing surface, related to the direct decomposition of SiH_4 and CH_4 in the plasma, as well as to the effect of the atomic hydrogen.

-When x>0.5, σ_d starts decreasing sharply while ΔE and E_{op} decrease more slowly. This can be explained by an increase of the defects created (shrinkage of E_{op}) ascribed with the manner in which carbon and boron are bonded to silicon species.

iii)*At high dp and dilutions ratios*

-When films are produced using high dp and doping levels (B_2H_6/SiH_4 and PH_3/SiH_4>1%) and SiH_4/H_2<3%, microcrystallization occurs. These films present high conductivities and low absorptions in the visible range. Their electro-optical properties are shown in Fig. 7, where we can see that, by changing the amount of carbon incorporated, control on E_{op} is achieved.

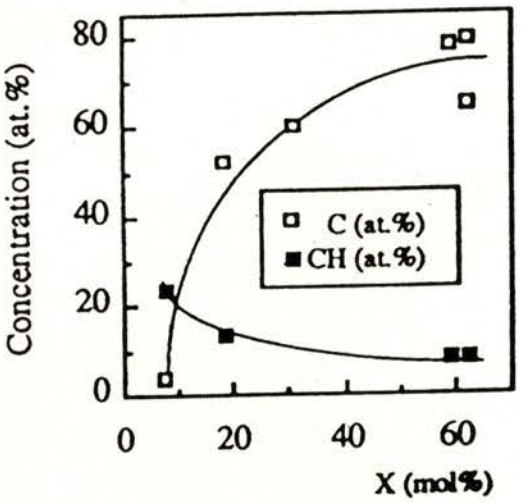

Fig. 4 - C_H and C_C as a function of x, for a -Si:C:H.

b) Structural properties

The way in which hydrogen and carbon are incorporated in the amorphous matrix depends strongly on dp and x values used, as we can see by the analysis of the IR spectra (Fig. 3):

i)At low dp

-Results presented in Fig. 3a) show that by keeping dp = 4 $mWcm^{-3}$ and changing x from 0.07 to 0.5 the peak ascribed with SiH_n (n=1,2,3) "wagging modes" is widened and shifted towards high wave numbers. They also show that a peak around 750 cm^{-1} (eventually attributed to Si:C stretching modes[8]) starts appearing. This reflects an effective incorporation of carbon in the matrix (as was confirmed by RBS and ESCA measurements), with hydrogen incorporated mainly in the form of =SiH (the contribution of the bending modes at 890 cm^{-1} attributed to dihydride species are kept at low levels). The wide band also observed between 2800 - 3000 cm^{-1} [8] whatever the x value used, confirms that CH_4 must be incorporated in the film, mainly as $-CH_3$ radicals.

ii)*At low x*

-In Fig. 3b) the behaviour of the bond configuration with dp for x=0.07 is shown. Here, we observe that there are no significant changes by increasing dp (the peak around 750 cm^{-1} does not appear). The most significant effect is the enhancement of CH with dp and the decrease of the bending modes ascribed to $=SiH_2$ species. This shows that SiH_n is mainly incorporated in the form of monohydride species, which are the main precursor of the growing process.

iii)*At high x*

-In Fig. 3c) we show the same dependence but with x=0.6 and in the presence of a high hydrogen flux. By increasing dp, a clear change in bond configuration is observed with the shift of the main peak from 630cm^{-1} to 750 cm^{-1}. At the same time, C_H decreases when dp increases to 140 $mWcm^{-3}$. This change is ascribed with the increase of C_C in the amorphous matrix (Fig.4) , mainly in tetrahedral bonds with Si atoms.

iv)*At high dp and dilutions ratios*

By heavily doping (B_2H_6/SiH_4 or PH_3/SiH_4>1%) these films and by using

a dilution ratio lower than 3%, microcrystallization occurs. The microstructure was determined by normal X-ray diffraction measurements and TEM analysis (Fig. 5).

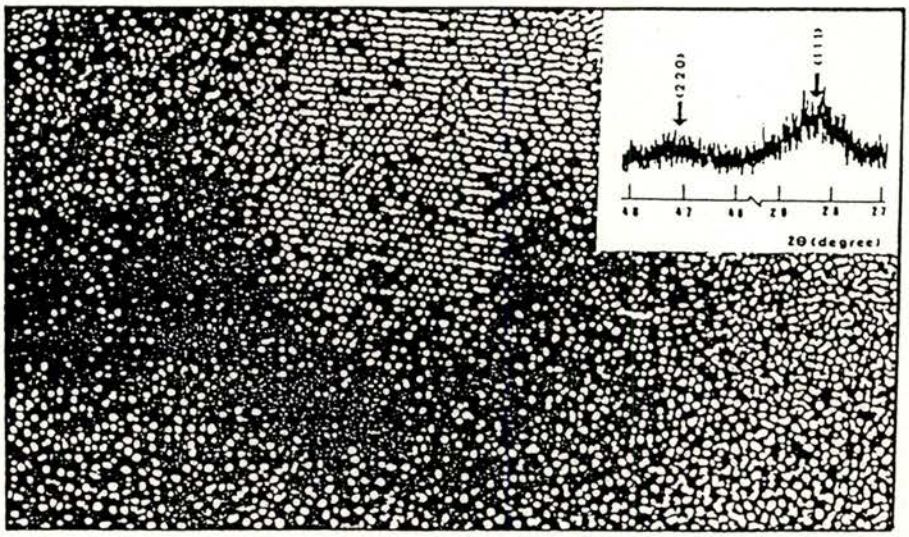

Fig. 5 - Cross-section transmission electron of n-type μc - Si:C:H. The insert show a typical X-ray pattern for the same film.

The carbon content was inferred by ESCA measurements as shown in Fig. 6, for a n-type sample.

The observed shift of the wagging modes from 630 cm^{-1} to 650 cm^{-1} on these films and the enhancement of the bending modes (Fig. 2c), are attributed to the incorporation of SiH_2 species in the grain boundaries of the microcrystallites [9]. From ESCA and RBS measurements we observe that C_C increases as x increases whilst C_H decreases from 19 to 4% [10]. Again, a good correlation between carbon atoms in the gas phase and that ones incorporated in the matrix are obtained, which explains the large E_{op} values recorded.

4-CONCLUSIONS

Overall, the experimental results show that the kinetics of the deposition process, for alloys, depend on the species involved and their affinities.

At low dp: CH_4 works as a buffer gas [11] (the power threshold for the decomposition of methane is higher than that of silane), since there is no primary decomposition of CH_4 and so, the incorporation of carbon in the films can only result from a chemical reaction between the "species" (SiH,SiH_2,SiH_3,H..), created by the plasma from SiH_4 and the CH_4 molecules. Hydrogen will be mainly in

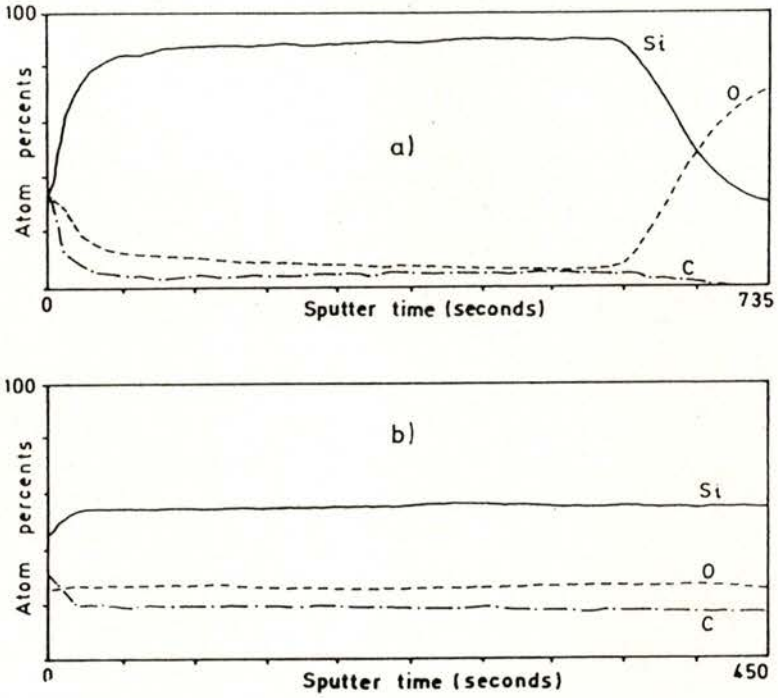

Fig. 6 - ESCA depth spectra for a n-type TCDDC SiC film.

corporated in the form of =SiH radicals or in methyl groups (-CH_3). It will then be more proper to name the amorphous silicon-carbon alloys "methylated amorphous silicon" (a-Si:CH_3:H). Due to chemical incorporation of carbon, this material shows the same properties of the a-Si:H, but has a large E_{op} associated to the existence of methyl groups randomly distributed in the amorphous tissue.

-At high dp: two different cases can occur:

i) If the applied power is high enough to decompose the CH_4 we get a SiC alloy with an effective incorporation of carbon much higher than those ones produced at low dp.

ii) If the gas mixtures are very diluted in H_2 (SiH_4/H_2<3%) and the r.f. power is enough to promote the production of atomic hydrogen, etching effects occur, which lead to the production of microcrystalline materials [9], as confirmed by X-ray diffraction measurements and TEM analysis. These results show that the material contains Si microcrystallites (Fig. 5) with grain size of the order of 100 angstrom, embedded in an amorphous silicon-carbon matrix. There is no evidence of SiC crystallites [10].

-Valence control: can be achieved either by changing the mixture composition (SiH_4+CH_4) or the dp used, for undoped and doped films. Undoped a-Si:C:H (σ_d <10^{-11} $\Omega^{-1}cm^{-1}$) are produced at low dp,

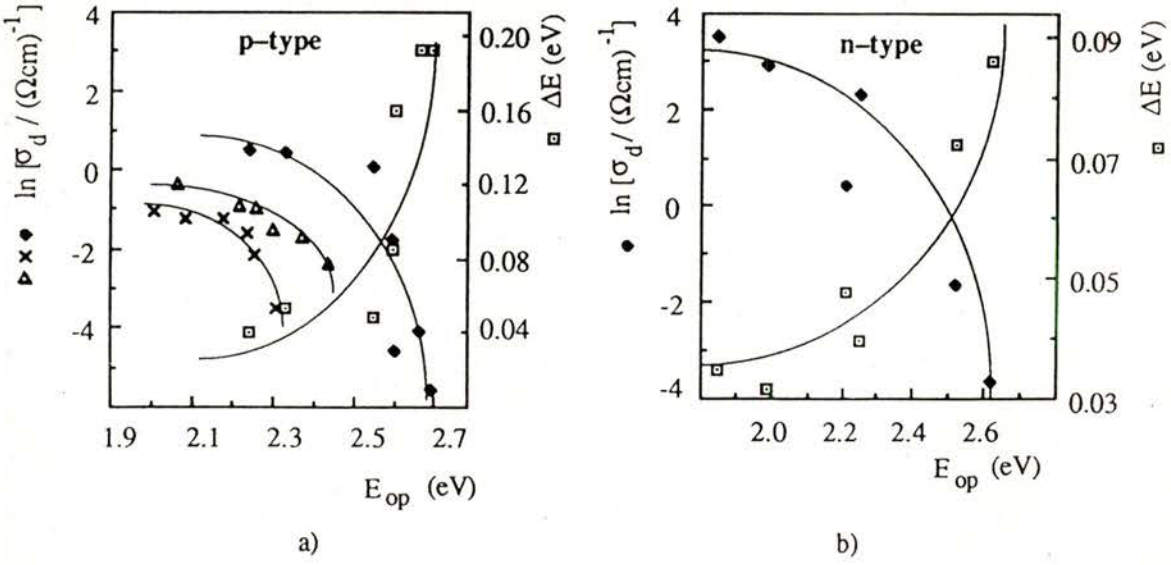

Fig. 7 - σ_d and ΔE as a function of E_{op} : a) p - type; b) n - type. We also show results for p - type films prepared by CPM (▲) and diode (×) methods.

being the growth process mainly ascribed to SiH precursors [6]. Undoped films produced with a SiH_4:CH_4 mixture in the ratio 1:5 present structural and transport properties (high resistivity/ low absorption) required for the production of blocking or dielectric layers, to be used on solar cells or TFT's devices.

On the other hand, doped μc-films highly conductive and weakly absorbing can be used as front/back contact on p.i.n solar cells in order to decrease absorption losses and to enhance carrier's collection in the blue range (when the back metal electrode is highly reflector), respectively.

ACKNOWLEDGEMENTS

The authors wish to express their thanks to Dr. G. Willeke (IMEC) for the help and contribution given during film's characterization and analysis of the obtained results.

This work was supported by Junta Nacional de Investigação Científica under project nº 87.618 and Instituto Nacional de Investigação Científica/Centro de Física Molecular das Universidades de Lisboa under project B.

REFERENCES

[1] Von Roedern, B., Proc. of 2nd Int. Seminar on Metal Organic and Plasma Assisted CVD, Florida, February 1988.

[2] Hamakawa, Y., "Current Topics in Photovoltaics", Academic Press Inc. (1985).

[3] Hattori, Y., Kruangam, D., Toyama, T., Okamoto, H. and Hamakawa, Y., Techn. Digest Int. PVSEC-3, Tokyo,Japan, Nov. 1987.

[4] Bauer, G.H. et al., Journal of Non-Crystalline Solid Films, vol.97&98, (1987), pp. 1415-1418.

[5] Pereyra, I., Journal of Non-Crystalline Solid Films, vol. 97&98, (1987), pp. 871-874.

[6] Martins, R., Guimarães, L., Fortunato, E., Vieira, M., Carvalho, N., Santos, M. and Ferreira, I., Proc. 8th EEC-PVSEC, Florence, Italy, May 1988, pp. 653-660.

[7] Vieira, M., Martins, R., Maçarico, A., Baía, I., Soares, F. and Guimarães, L., on the Proc. of MRS Spring Meeting Conference on Reno, Nevada, U.S.A., April 1988, vol. 118, pp. 113-116.

[8] Tawada, Y., Proc. of Inter. Soc. for Optical Eng. Conf. 706 (Cambridge-1974).

[9] Veprek, S., Winter European Course on Amorphous Silicon, Italy, February 1988.

[10] Willeke, G. and Martins, R., presented at the 24th IEEE-PVSEC, Las Vegas, Nevada, U.S.A., September 1988, to be published.

[11] Solomon, I., Winter European Course on Amorphous Silicon, Italy, February 1988.

OPTOELECTRONIC PROPERTIES PRESENTED BY DOPED AND UNDOPED AMORPHOUS SILICON FILMS

S. SOALHEIRA, R. MARTINS, C. CARVALHO, I. BAÍA AND L. GUIMARÃES
Faculdade de Ciências e Tecnologia da Universidade Nova de Lisboa
Quinta da Torre, 2825 Monte da Caparica, Portugal

ABSTRACT -This work deals with transport and structural properties of undoped and doped a-Si:H films produced by plasma enhanced chemical vapour deposition techniques and their dependence on deposition conditions. Namely, the effect of plasma conditions substrate temperature (T_s), deposition pressure (p) and power used (P), on dark conductivity (σ_d), optical gap (E_{op}), activation energy (ΔE), photosensitivity (σ_{ph}/σ_d) and the way in which the [SiH], [SiH_2] and [SiH_3] species are incorporated, will be discussed. Overall we observe that undoped films with good performances are obtained when during the deposition process T_s=260 C, P=10 - 20 W and p=0.1 Torr. As far as doped films are concerned, the best film performances are obtained using p=0.5 Torr and high dilution ratios of silane in hydrogen. We also studied the behaviour of a-Si:C:H alloys based on methane/silane mixtures, doped or not with boron and produced at low powers ($P \simeq 5W$).

1. INTRODUCTION

Since Spear in 1975 [1] doped effectively a-Si:H films, the interest in using such semi-conductors in several photovoltaic and nonphotovoltaic applications has been growing . Nevertheless, most of the work done is based on trials that experience demonstrates to lead to films with good performances for their particular applications. Most of the problems concerned with films produced for device applications are due to the way in which hydrogen is incorporated and with density of states (DOS) within the mobility gap.

In this work we intend to determine the best deposition conditions that lead to the production of stable a-Si:H films with optoelectronic properties suitable for producing photovoltaic devices. This will be done either for films produced by conventional diode or by TCDDC (Two Consecutive Decomposition and Deposition Chamber) systems, respectively.

2. EXPERIMENTAL ANALYSIS OF THE PLASMA

Priori to deposit a-Si:H films, Paschen curves [2] corresponding to plasma discharges on hydrogen and silane were taken in order to characterize the plasma. In Fig.1 we show the behaviour of four of those typical Paschen curves.

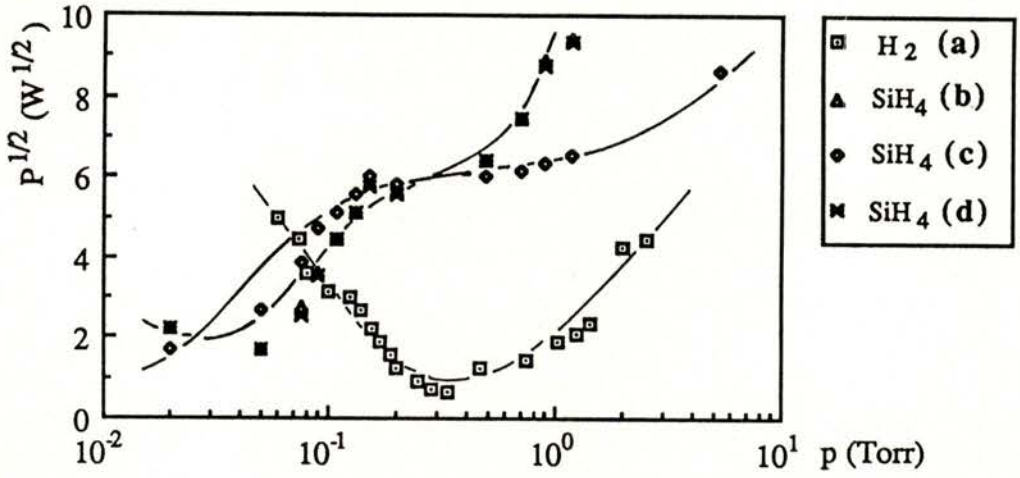

Fig. 1 -Paschen Plots for H_2 (a) and for silane at different electromagnetic static films (b: I_B=0, V_G=- 50 V; c: I_B= 3 A, V_G=- 50 V; d: I_B=0, V_G=0 V).

This study allows us to determine the minimum potential needed to obtain the glow, and so, the power that we must use in order to promote plasma formation, as well as to separate the high pressure from the one of low pressure (e.g. the kind of collisions undertaken by the formed species) [3]. Besides this, we also inferred the behaviour of such curves under electromagnetic crossed static fields [4],[6]. From this analysis, we see that the presence of a dc bias voltage (V_G) and a magnetic static field (I_B) during plasma formation, shifts the minimum of Paschen curves towards lower pressures. We also observe that the minimum of Paschen curves for H_2 discharges is ascribed with pressures almost one order of magnitude higher than the one for silane. This means that hydrogen when present during the discharge process acts mainly as a "buffer-gas" since the threshold of decomposition is superior to that one of silane, at low pressures. Once defined the best plasma conditions, we determine the correlation between power used and growth rate, either for undoped or doped a-Si:H films. These results are shown in Fig.2, where we observe that, by diluting carrier gas in hydrogen, the growth rate decreases by a factor of seven when $SiH_4/H_2 < 5\%$.

3. EXPERIMENTAL DETAILS

The films analyzed were produced by plasma enhanced chemical vapour deposition either using a diode-type system

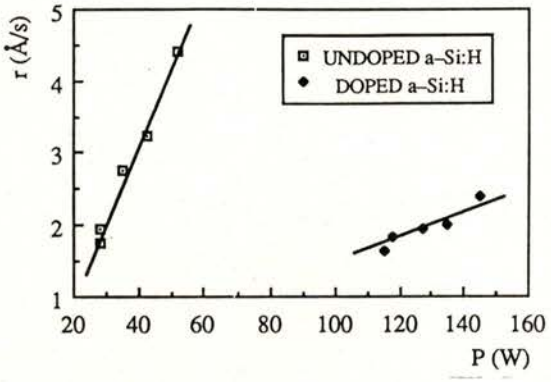

Fig.2 - Growth rate as a function of power used for undoped (□) and doped (♦) (with $Si_4H_2 < 5\ \%$) for a-Si:H films.

or TCDDC system, where plasma chemistry is separated from that one of the deposition [4]. The obtained films were grown on glass substrates. Dark conductivity and photoconductivity measurements were performed on films using a gap-cell electrode configuration. Optical gap was inferred from Tauc's plot [4] through the absorbance measurements obtained by a double beam spectrophotometer. Hydrogen content was inferred through IR measurements performed on films grown onto high resistivity policrystalline silicon wafers.

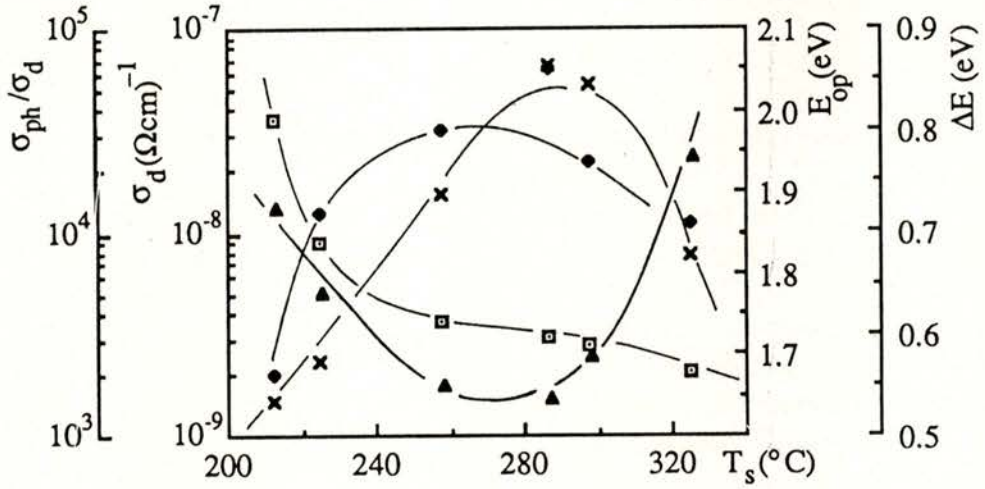

Fig.3 - The dependence of σ_d (▲), σ_{ph}/σ_d (×), ΔE (◆) and E_{op} (□) on substrate temperature used for undoped a-Si:H films.

4. RESULTS AND DISCUSSION

a) Effect of substrate temperature:

In Fig.3 we show the dependence of σ_d and σ_{ph}/σ_d on substrate temperature used for undoped a-Si:H films produced at discharge pressures of the order of 0.2 Torr and constant powers. There, it is

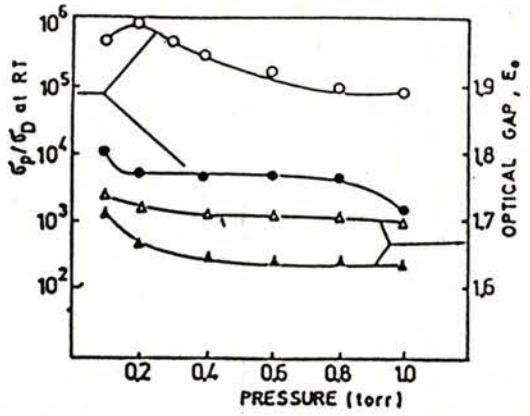

Fig. 4 - Dependence of σ_{ph}/σ_d and E_{op} on p for undoped films deposited by TCDDC system (o) and by a conventional diode-system (o).

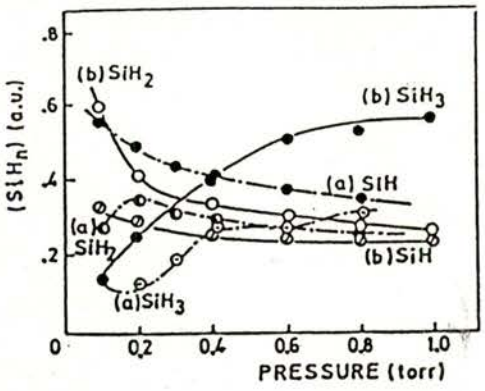

Fig. 5 - Dependence of species concentration (arbitrary units) on p, a) Films deposited by TCDDC system. b) Films deposited by a conventional diode-system.

also shown the corresponding behaviour of the optical gap, E_{op} , and of the activation energy, ΔE. The results show that σ_d has its minimum at substrate temperatures of the order of 260 C, which corresponds to the maximum in σ_{ph} /σ_d with $\Delta E \simeq 0.8$ eV and $E_{op} \simeq 1.73$ eV, at T_s=260 C. For $T_s \gtrsim 260$ C, σ_d increases while σ_{ph} /σ_d decreases. From the obtained results we see that:

- at substrate temperatures, T_s , below 260 C there is a high hydrogen incorporation related to a high DOS [1] which is responsible for the high E_{op} and σ_d results obtained as well as the low σ_{ph} /σ_d values recorded.
- at T_s above 260 C σ_{ph} /σ_d decreases and σ_d increases, while E_{op} remains almost constant. This is explained by the decrease in hydrogen content on the film as well as by the reduction on $\mu\tau$ product [5].

b) Effect of the pressure:

In Fig. 4 we show the dependence of σ_{ph}/σ_d and E_{op} on the deposition pressure, p, for films deposited at T_S = 260 C by a TCDDC system (open circles) and by a conventional diode-system (dark circles). The data show that films produced by the TCDDC system have photosensitivities more than one order of magnitude higher than those ones produced by the conventional system [6]. The best σ_{ph} /σ_d are obtained for p in the range of 0.1-0.2 Torr, which to corresponds values of the order of 10^6 (with $E_{op} \simeq 1.73$ eV) for the TCDDC system and of the order of 10^4 (with E_{op} 1.65 eV) for the conventional diode-system. In Fig.5 we also show the qualitative dependence of species concentration (deduced from IR spectra) on p, ei-

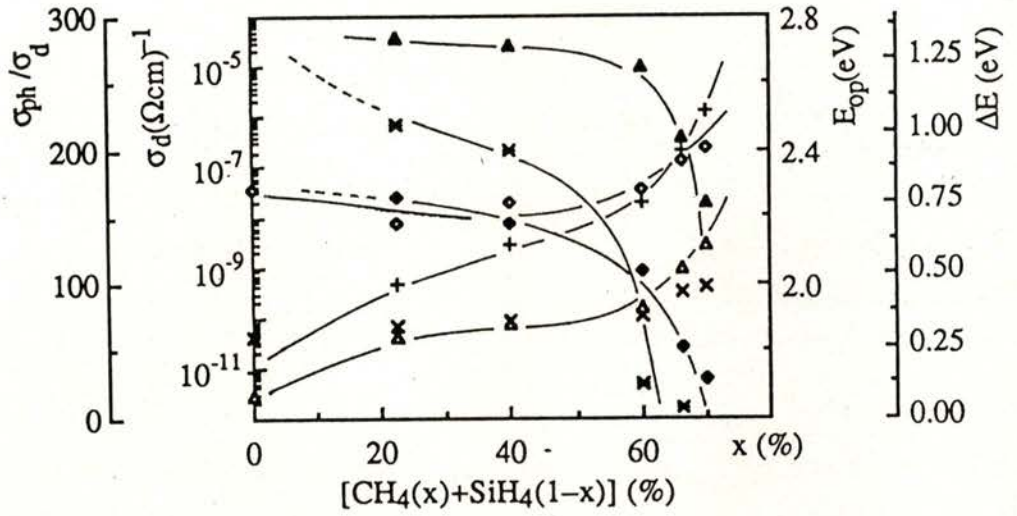

Fig. 6 - The dependence of σ_{ph}/σ_d (✱),σ_d (◆,▲), E_{op} (+,▲) and ΔE (◆,x) on the dilution ratio used for undoped (a-Si:C:H (✱,◆,+,◇)) and doped (a-Si:C(B):H (▲,△, x)) samples produced at low powers, respectively.

ther for the TCDDC system (a) or the conventional diode-system (b). There, we observe that species incorporation is dependent on pressure used, being the main percurssor ascribed to SiH species, for TCDDC system, and, with SiH_2 species for the conventional diode system. For pressures below 0.2 Torr, the ratio between [SiH]/[SiH_2] is higher than a factor of nine for films produced by the TCDDC system.

c) Performances presented by a-Si:C:H doped and undoped alloys:

In Fig. 6 we show the dependence of σ_{ph}/σ_d, σ_d, E_{op} and ΔE on the ratio x = [CH_4/(SiH_4 + CH_4)] used, for undoped and doped samples produced at low powers (P≃ 5 W). Overall we see that:

- E_{op} increases as x increases while σ_d decreases behind the detectable limits of the apparatus used. The same happens with σ_{ph}/σ_d.
- As far as doped samples with 1% of boron are concerned, E_{op} also increases with x, but more slowly. ΔE presents values between 0.25 and 0.4 eV while σ_d though higher than that one for undoped samples, it still decreases as x increases.

d) Behaviour of phosphorous doped samples:

In Fig. 7-a) we show the dependence of σ_d, E_{op}, and ΔE on the dilution ration (y = H_2/SiH_4) using P > 100 W and p = 0.5 Torr. Overall we observe that for 0 < y < 10, σ_d decreases while ΔE and Eop are

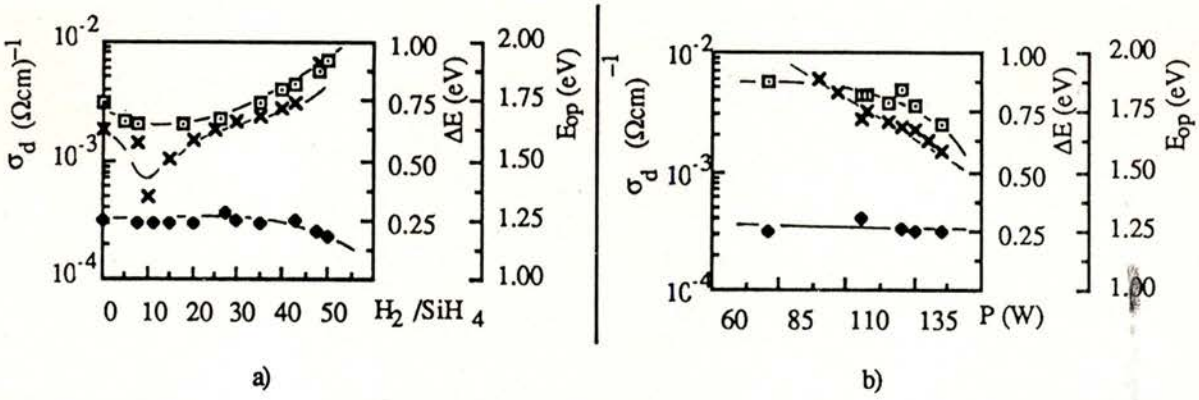

Fig. 7 - a) Dependence of σ_d (×), E_{op} (□) and ΔE (◆) on H_2/SiH_4. b) The same dependence as a function of the power used.

kept almost constant, For y >10, σ_d starts increasing while ΔE and E_{op} present significant changes for y > 35 (ΔE decreases and E_{op} increases). This means that the dilution of the carrier gas in hydrogen will improve the optoelectronic performances of doped films, and so, that film properties are dependent on the residence time of hydrogenionic species present during the discharge process [4]. In Fig. 7-b) we show the same dependence as above but for the power used, having p = 0.5 Torr and y≥30. The obtained data show a decrease in σ_d and E_{op} as P increases while ΔE is kept almost constant. This can be explained by the ionic bombardment of the growing surface that will enhance the number of DOS, whilst the number of active species incorporated in active matrix, decreases. Similar behaviour was observed for boron doped films.

5. CONCLUSIONS

1 - Plasma behaviour during the deposition process can be determined by knowing the corresponding Paschen curves. Indeed, as low as the potential needed to promote plasma ignition as less as will be the effect of ionic bombardment on the growing surface. This means that for producing good quality material, the power at which the plasma is produced must be at or near the minimum of the Paschen curves.

2 - Overall we observe that deposition conditions play a significant role on film performances. Concerning T_s, the best value that leads to undoped films with good optoelectronic properties is in the range of 250-260 C, while 0.1 < p <0.2 Torr.

3 - a-Si:C:H undoped and boron doped films present valence controllability by changing the composition of methane/silane mixtures. High optical

gaps and high resistivities are obtained (for undoped films) in rich methane mixtures.

4 - For amorphous doped films, good optoelectronic properties are obtained by using low P and high hydrogen dilutions. As the power increases, the growing surface is under intense bombardment which enhances DOS and so leads to poor quality films. This is related to the residence time of species during the growth process [4]. Thus, for getting good doped films at high powers, the growth surface must be under atomic hydrogen bombardment and the residence time must be higher than the reaction time, in order to promote plasma chemical equilibrium conditions [3], which can lead us to mycrocrystallization.

5 - The species incorporated depend on reactor used. [SiH] and [SiH_2] species are assigned as being the main percursors for films produced by TCDDC and conventional diode type systems, respectively.

6 - We also observe that films produced by the TCDDC system present better performances than those ones produced by the conventional diode-system.

Acknowledgements

The authors would like to thank A. Maçarico, M. Santos and R. Leal for the help given during film preparation and characterization. This work was supported by Instituto Nacional de Investigação Científica/Centro de Física Molecular das Universidades de Lisboa.

REFERENCES

[1] Spear, W. E. and Le Comber, P. G., Phil Mag., Vol. 33, **6**, 935-949 (1976).

[2] Von Engel, A., Ionized Gases, Second Edition, Oxford at the Clarendon Press.

[3] Veprek, S., et. al., J. de Physique, **42 C4**, 251 (1981).

[4] Martins, R. and Guimarães, L. Proc. of 5th E.C. Photov. Solar En. Conf. (Athens 1983), 146; Martins, R., et. al., "Performances Presented by a-Si:C:H Films produced by a TCDDC System for PV Applications" (invited), Proc. of 8th E.C. Photovoltaic Solar En. Conf. (Florence 1988).

[5] Hamakawa, Y., "Amorphous Silicon Solar Cells", Current Topics in Photovoltaics, **3**, 111 (1985).

[6] Martins, R., Dias, A. G. and Guimarães, Portugal. Phys. - **14**, fasc. 1-2 , 81-94 (1983).

SEMICONDUCTOR PROPERTIES OF THE EARTH'S CORE

FREDERICO MACHADO
Centro de Geofísica, R. Esc. Politécnica, 58, 1200 Lisboa Portugal

ABSTRACT-Assuming that the Earth's core consists of a nickel-iron oxide, which is certainly a semi-conductor, some relevant electrical properties of such material are presently discussed. Under convenient conditions, the actual geomagnetic field can be generated by a small rotation of the solid inner core in relation to the mantle.

1. INTRODUCTION

It is currently believed that the material in the Earth's core is a nickel-iron alloy (for e.g. $Fe_{0.9}Ni_{0.1}$,) with addition of an element of lower atomic weight. For some time, this additional element was supposed to be sulphur, but now oxygen is receiving considerable favour [1,2].
As iron oxides are semiconductors, the hypothesis gives the core remarkable electrical properties and suggests an adequate mechanism for generating the geomagnetic field [3]. This appears to be a promising alternative to the self-exciting dynamo which is currently accepted, but could not yet receive a quantitative treatment [4].

2. THERMOELECTRIC PROPERTIES OF SEMICONDUCTORS

In a semiconductor, electric current is due to the movement of both electrons and holes. With n electrons and p holes the flow of electric charge is

$$j_q = (n\mu_e + p\mu_h)eE \qquad (1)$$

where μ_e, μ_h are, respectively the mobilities of electrons and holes; e is the elementary charge and E is the electric field [5].
On the other hand, semiconductors are characterized by their energy bands (Fig. 1). Let E_c be the lowest point of the conduction band, and E_v the highest point of the valence band.
The energy gap is

$$E_g = E_c - E_v \qquad (2)$$

and the Fermi level ε_F lies in this gap so that we can write

$$\varepsilon_F = E_v + f\,E_g \qquad (3)$$

with $0 < f < 1$.

At absolute zero, the conduction band is vacant and the valence band completely filled. As temperature rises, some electrons from the valence band are excited and pass into the conduction band. Following Kittel [5], we assume that the electrons acquire an energy $E_c - \varepsilon_F$ and the holes, which are left behind in the valence band, acquire energy $\varepsilon_F - E_v$. In both cases we must add the thermal energy $\frac{3}{2} k_B T$, T being the temperature and k_B the Boltzmann constant.
The total flow of energy will then be

$$j_U = - n\mu_e(E_c-\varepsilon_F+\frac{3}{2}k_BT)E+p\mu_h(\varepsilon_F-E_v+\frac{3}{2}k_BT)E \quad (4)$$

Dividing by the flow of charge given by (1), we get Peltier's coefficient

$$\Pi = \frac{j_U}{j_q} = \frac{[M(f-1)+f]E_g - \frac{3}{2}(M-1)k_BT}{(M+1)e} \quad (5)$$

where $M = n\mu_e / p\mu_h$ and use was made of eq. (3). In the intrinsic temperature range we have n=p and therefore $M = \mu_e / \mu_h$.
At least for moderate intervals of temperature, M, f and E_g can be assumed as independent of T and we can write

$$\Pi = A + BT \quad (6)$$

the constants A and B being

$$A = \left(f - \frac{M}{M+1}\right)\frac{E_g}{e} \qquad B = -\frac{3}{2}\frac{M-1}{M+1}\frac{k_B}{e} \quad (7)$$

The presence of a thermal gradient will produce, within the semiconductor, the electric field

$$E = - \text{grad } V = \frac{\Pi}{T} \text{grad } T \quad (8)$$

where V is the electrostatic potential.
The scalar product of (8) by the elementary length gives

$$- dV = \frac{\Pi}{T} dT \quad (9)$$

or, using (6),

$$dV = -\left(\frac{A}{T} + B\right) dT \quad (10)$$

which integrates into

$$V - V_0 = - A \ln \frac{T}{T_0} - B(T - T_0) \quad (11)$$

V_0 and T_0 being integration constants that make $V = V_0$ when $T = T_0$.

3. THOMAS-FERMI APPROXIMATION

As between E_v and ε_F (Fig. 1) there are no allowed orbitals, E_v can be computed by the expression, which gives ε_F in metals,

$$E_v = \frac{h^2}{8\pi^2 m}(3\pi^2 n)^{2/3} \quad (12)$$

Here h is Planck´s constant, m is the electronic mass and n is now the free electron concentration.

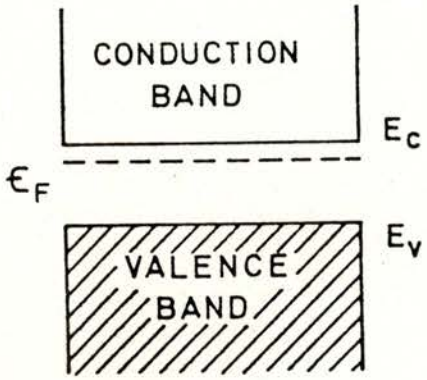

Fig. 1 - Energy bands of a semiconductor. At absolute zero, the conduction band is empty and the valence band completely filled.

The chemical potential can be defined as

$$U = \varepsilon_F(n) - e(V - V_0) \qquad (13)$$

where V_0 is a constant to be determined. If n_0 is the concentration when $V = V_0$ we have then $U = \varepsilon_F(n_0)$.

According to the Thomas-Fermi approximation, the chemical potential must be constant for any part of a substance in thermal and diffusive equilibrium [5]. Therefore

$$\varepsilon_F(n) - e(V - V_0) = \varepsilon_F(n_0) \qquad (14)$$

Expanding $\varepsilon_F(n)$ in a Taylor series, we get

$$\varepsilon_F(n) = \varepsilon_F(n_0) + \left(\frac{d\varepsilon_F}{dn}\right)_{n=n_0} (n - n_0) + \ldots \qquad (15)$$

Substituting in (14) and neglecting powers of $n - n_0$ of second or higher order, we obtain

$$n - n_0 = \frac{e}{(d\varepsilon_F / dn)_{n=n_0}} (V - V_0) \qquad (16)$$

Using (3), with $f E_g$ constant,

$$\frac{d\varepsilon_F}{dn} = \frac{dE_v}{dn} \qquad (17)$$

Now, taking logarithms of both members of (12) and differentiating, we have

$$\left(\frac{d\varepsilon_F}{dn}\right)_{n=n_0} = \frac{2E_v(n_0)}{3n_0} \qquad (18)$$

and with this value (16) becomes

$$n - n_0 = \frac{3en_0}{2E_v(n_0)} (V - V_0) \qquad (19)$$

Multiplying by - e and using (11), we obtain finally the density of charge

$$\rho = -e(n - n_0) = \frac{3e^2 n_0}{2E_v(n_0)} \left[A \ln \frac{T}{T_0} + B(T - T_0)\right] \qquad (20)$$

n_0 and T_0 being constants to be determined.

4. MODEL OF THE CORE

For the present computations we shall use the PREM model [6], which has the following dimensions:-

Radius of the inner core: $R_1 = 1221.5$ km
Radius of the outer core: $R_2 = 3480$ km

The density (in g/cm^3) of the outer core is described by the polynomial

$$d=12.5815 - 1.2638\,\frac{r}{R} - 3.6426\left(\frac{r}{R}\right)^2 - 5.5281\left(\frac{r}{R}\right)^3 \qquad (21)$$

r being the radius at each level and R = 6371 km being the mean radius of the Earth.

As what concerns chemical composition, we extended Ringwood's ideas [2] by assuming that both the solid inner core and the molten outer core are formed by the oxide $Fe_{0.9}Ni_{0.1}O_{0.5}$. The corresponding kg-molecule is M_{mol} = 64.125 kg.

This material is certainly a semiconductor, to which we attributed tentatively the following properties:-

$$M = 1.2 \qquad f = 0.8 \qquad E_g = 0.4\ eV$$

It is a p-type semiconductor (because Peltier's coefficient is positive). Within a first approximation, we assume that eq. (20) also applies (with the same parameters) to the molten core material.

5. ROTATION AND TEMPERATURE

The actual rotation of the Earth's mantle must convey the whole core; but, as the inner core is separated from the mantle by a thick liquid layer, its rotation could be slightly advanced or retarded in relation to the mantle.

It was previously proposed [3] that the relative angular velocity of the inner core is expressed in the westward drift of the geomagnetic field. The determination of this drift is somewhat difficult; an approximate mean value is $\omega_1 = -1.0*10^{-10}$ rad/s [7,8].

The relative angular velocity ω must decrease in the molten outer core, vanishing at the mantle-core boundary. The variation is given approximately by the equations

$$\frac{\omega}{\omega_1} = 1 \qquad \text{for} \quad r < R_1$$

$$\frac{\omega}{\omega_1} = \frac{R_1^\beta}{R_2^\beta - R_1^\beta}\left(\frac{R_2^\beta}{r^\beta} - 1\right) \qquad \text{for } R_1 < r < R_1 \qquad (22)$$

β being a function of the viscosity of the molten material [9]. We made β = 7.39 which corresponds to a viscosity of about 10^4 Pa.s. A graph of eq. (22) is shown in Fig. 2.

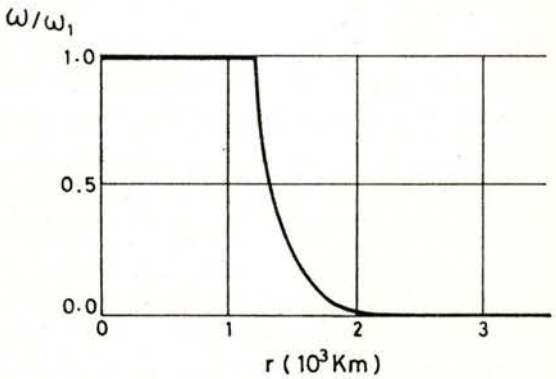

Fig. 2 - Variation of angular velocity in the Earth's core (relative to the mantle). Viscosity of the outer core was assumed to be about 10^4 Pa.s.

In this model, the temperature at the boundary between inner and outer core

must be the melting point of the material. We are using the value of 5000 K, as proposed by Poirier [10].
As to what concerns the thermal gradient, it is believed that the content of radioactive elements (assumed to be similar to the content in iron meteorites) is too small for producing an adiabatic gradient. If heat is transmitted only by conduction, the temperature must satisfy the equation

$$\text{lap } T = -\frac{H}{K} \qquad (23)$$

H being the radioactive heat production per unit volume and k the thermal conductivity.
Assuming spherical symmetry, and constancy of H and k throughout the core, integration of (23) gives

$$T = 5000 + \frac{H}{6k}(R_1^2 - r^2) \qquad (24)$$

Here $T = 5000$ K for $r = R_1$, as initially postulated.

6. GENERATION OF THE GEOMAGNETIC FIELD

As the Earth's core, taken as a whole, is thought to be in a neutral electrical state, the total charge must be zero, i.e.

$$4\pi \int_0^{R_2} \rho r^2 dr = 0 \qquad (25)$$

Noting that for H/k small we have approximately $\ln(T/T_0) = (H/6k)(r_0^2 - r^2)/5000$ (with $r = r_0$ for $T = T_0$), and substituting from (20) we get

$$\int_0^{R_2} (r_0^2 - r^2)\, r^2 dr = 0 \qquad (26)$$

giving (for the assumed model) $r_0^2 = 3R_2^2/5$. The concentration n_0 will be

$$n_o = \frac{N d_0}{M_{mol}} \qquad (27)$$

where N is the Avogadro constant and d_0 a density obtained from (21). We get $r_0 = 2695.6$ km, $d_0 = 10.99$ g/cm^3, $n_0 = 1.032 * 10^{29}$ m^{-3} and $E_v(n_0) = 8.02$ eV; and we now have all the constants which appear in eq. (20), except for H/k which is included in T.

The magnetic moment of the Earth is, approximately,

$$M_{mgn} = \frac{4\pi}{3} \int_0^{R_2} \rho \omega r^4 dr \qquad (28)$$

and can be computed by direct substitution of (20) and (22) (using for $\ln(T/T_0)$ the approximation indicated above).
The value of the moment is $M_{mgn} = -7.94 * 10^{22}$ Am^2, referred to the 1975 geomagnetic field [11]. The factor H/k of eq. (24) can be chosen for having this value of M_{mgn}.

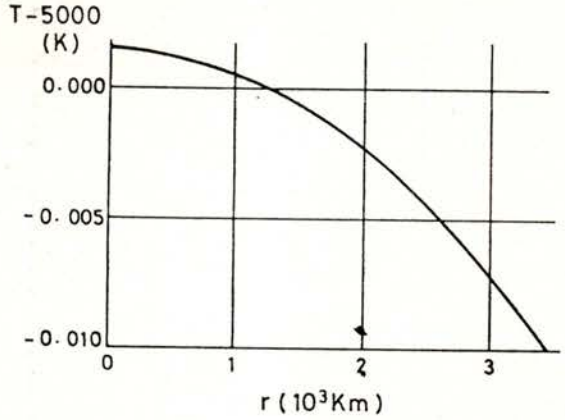

Fig. 3 - Variation of temperature in the Earth's core, with $H/k = 5.66*10^{-9}$ K/km^2. Heat transmission is supposed to be by conduction only.

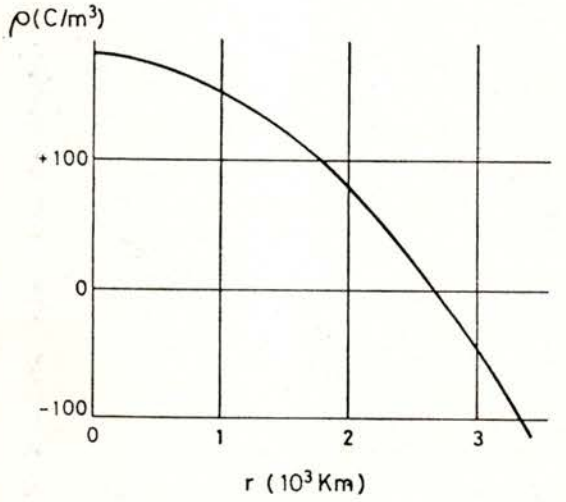

Fig. 4 - Variation of electric charge density in the Earth's core. The values were obtained as described in the text.

For the material described in section 4, we obtained $H/k = 5.66*10^{-9}$ K/km^2, which is a value in the magnitude range of iron meteorites. The corresponding temperatures are shown in Fig. 3 and the charge densities in Fig. 4.

These results indicate that the proposed mechanism is a good possibility, but the actual composition and properties of the core model have certainly to be improved by laboratory research.

ACKNOWLEDGEMENTS

The writer is indebted to L. Mendes Victor for critically reading the manuscript; and to M. Graça Marques for preparing the drawings. The present research was partly supported by a grant from Instituto Nacional de Investigação Científica, in Lisbon.

REFERENCES

[1] Bullen, K. E., Nature (London), **243**, 68 (1973).
[2] Ringwood, A. E., The Earth, Its Origin, Structure and Evolution (M. W. McElhinny, ed.), chapter 1, Academic, New York (1979).
[3] Machado, F., Mem. e Notícias (Univ. Coimbra), **99**, 127 (1985).
[4] Jacobs, J. A., The Earth's Core, 2nd ed., chapter 5, Academic, London (1987).
[5] Kittel, C., Introduction to Solid State Physics, 5th ed., chapters 8 and 10, Wiley, New York (1976).
[6] Dziewonski, A. M. and Anderson, D. L., Phys. Earth Planet. Inter., **25**, 297 (1981).
[7] Garland, G. D., Introduction to Geophysics, 2nd ed., 246, Saunders, Philadelfia (1979).
[8] McElhinny, M. W., Palaeomagnetism and Plate Tectonics, 7, Univ. Press, Cambridge (1973).
[9] Machado, F., Geociências (Univ. Aveiro), **5** (in press); Mem. e Notícias (Univ. Coimbra), **109**, 105 (1990).

[10] Poirer, J. P., Geophys. J. R. Astron. Soc., **85**, 315 (1986)

[11] Stacey, F. D., Physics of the Earth, 2nd ed., page 211, Wiley, New York (1977).

ELECTRONIC CORRELATIONS IN ONE-DIMENSIONAL CONDUCTORS

JOSÉ CARMELO[1,2], LUIZ CARLOS[1] AND ROSÁRIO MARTINS[2]

[1]Department of Physics, University of Évora, Ap. 94, P-7001 Évora Codex, Portugal

[2]Centro de Física da Matéria Condensada, Av. Prof. Gama Pinto, 2, P-1699 Lisboa Codex, Portugal

ABSTRACT-In this paper we use the variational Gutzwiller wave function to study the effects of the Coulomb electronic repulsive correlations on the plasma frequency and spin magnetic susceptibility of the Hubbard chain.

Our results agree with experimental data for quasi-one-dimensional conductors: on the one hand the plasma frequency is reduced by the electronic correlations and on the other hand these correlations lead to an enhancement of the spin magnetic susceptibility.

1. INTRODUCTION

The strong interest in synthetic metals started in the early seventies with the advent of TTF-TCNQ [1].

Many of these materials are highly anisotropic in their electrical properties and thus often referred to as "quasi-one-dimensional electronic systems". Such quasi-one-dimensionality follows from their structure, which is typically an array of rather weakly interacting metallic chains.

In the case of the organic crystals [2], [3], the electronic conduction takes place along stacks of planar organic molecules. These molecules, which are the elementary units of the linear chains, have a π-electron orbital which is oriented in the direction perpendicular to the plane of the molecule and allows for overlap between π-orbitals of adjacent molecules and thus for electrical transport.

The π-orbitals of the linear chains can either receive electrons from donor molecules or give electrons to acceptor molecules. These processes allow changing of the electronic density $n=N/N_a$ where N and N_a are the numbers of conducting electrons and sites of the linear chain.

When the electronic band, formed through the overlap between π-orbitals, is partially filled, the organic crystals behave as narrow band one-dimensional conductors.

The electronic structure of simple metals and alloys is in most cases well described by effective one-electron models where electron-electron interactions are taken into account through a self consistent field. This leads to the well-known model of Bloch for the conduction bands of metals and alloys.

Nonetheless, there is experimental evidence that in the case of the novel non-

trivial conductors and superconductors, as for example the just mentioned synthetic metals and the high T_c superconductors [4], the simple one-electron models are not sufficient to explain the electronic structure. These novel materials have in common the occurrence of low-dimensional effects (one and two dimensional) which imply a much more important role for the electron-electron interactions.

In the case of the organic quasi-one-dimensional metals the experimental values of the inverse of the plasma frequency and of the spin magnetic susceptibility, for example, are clearly enhanced in relation to those predicted by the model of Bloch [2],[3].

In this paper we use the one-dimensional Hubbard model [5] to describe the conducting π-electrons of the linear chains. The model is presented in Section 2. In Section 3 we apply the Gutzwiller variational scheme [6] (which was recently extended to the case of attractive correlations by one of us [7]) to evaluate the plasma frequency and spin magnetic susceptibility expressions. Section 4 gives a brief summary.

While the results concerning the spin magnetic susceptibility have not been published elsewhere, a previous study about the correlation effects on the oscillator strength of optical absorption was presented in Reference [8].

2. THE ONE-DIMENSIONAL HUBBARD MODEL

The structure of many synthetic metals can be represented by an array of weakly interacting chains. In the present work we neglect the interaction between the chains, which can be introduced as a small perturbation.

We consider N_a identical molecules at positions $x_j = j\,a = j$, $j = 1, \ldots\ldots\ldots, N_a$ (we use units such that the lattice constant $a = 1$). The molecular Wannier wave function for a conducting electron at site x_j and with spin σ ($\sigma = \pm\frac{1}{2}$) is denoted by $\phi_\sigma(x - x_j)$. We restrict our study to electronic densities such that $n \leq 1$ (the results for $n>1$ are readily obtained if one replaces electrons by holes). Moreover we only take into account the overlap between nearest neighbours electronic wave functions $\phi_\sigma(x - x_j)$ and $\phi_\sigma(x - x_{j+1})$. The hopping or transfer integral is given by:

$$t_{j,j+1} = t_{j+1,j} = t = \int dx\, \phi^*(x - x_j)\left[-\frac{\hbar^2}{2m}\frac{d^2}{dx^2} + V(x)\right]\phi(x - x_{j+1}) \quad (1)$$

where m is the electronic mass and V(x) is the lattice potential.

The square of the transfer integral (1) is related to the probability for electronic hopping between nearest neighbour sites.

The one-particle model obtained by the choice $t_{j,j+1} = t$ = constant, can be easily diagonalized, describing N conducting electrons in a band of width 4 t given by:

$$E(k) = -2\,t\cos(k) \qquad (2)$$

where the k momentum values are restricted to the first Brillouin zone, $|k| < \pi$. In the ground state only the orbitals with $|k| < k_F$ and spin projections $\sigma = \pm\frac{1}{2}$ are occupied (the one-dimensional Fermi surface is reduced to the two points $\pm k_F = \pm(\pi n)/2$).

The Hubbard model [5] contains, besides the hopping-term corresponding to the one-particle Hamiltonian described above, a many-body electronic potential which takes into account the Coulomb repulsive interaction between electrons on the same lattice site. Despite the drastic assumptions involved neglecting the long-range forces of the Coulomb repulsion, the Hubbard Hamiltonian has been quite successful in describing essential features of interacting electrons. The success of this model in describing, for example, some of the aspects of the physics of the novel synthetic metals is partially due to the screening of the long-range forces [9].

Besides the transfer integral (1), the Hubbard model includes the onsite repulsion parameter U,

$$U = \int dx\,dx' \phi^*_\sigma(x-x_j)\phi^*_{-\sigma}(x'-x_j)\frac{e^2}{|x-x'|}\phi_\sigma(x-x_j)\phi_{-\sigma}(x'-x_j) \qquad (3)$$

which is positive and measures the energy required to have two electrons of opposite spin projection on the same site.

The Hubbard model can describe two limiting situations. On the one hand for $U = 0$, the electrons are delocalized and have band-like behaviour. On the other hand for $U \gg t$, the weight of the electronic configurations showing double occupancy is drastically reduced, which implies a tendency for localization and antiferromagnetism if the density n is close to 1. In fact, in the particular case of the half-filled band, $n = 1$, the number of electrons N equals the number of lattice-sites N_a, and no double occupancy implies the full localization of the electrons.

In the intermediate regions ($U \simeq t$) we expect a cross-over from band-like to localized behaviour. This is the most interesting regime for the physics of the synthetic crystals, which show simultaneously metallic behaviour and properties which indicate a clear tendency for localization.

In second quantization the Hubbard model reads:

$$\hat{H} = -t\sum_{j,\sigma}[c^+_{j\sigma}c_{j+1\sigma} + c^+_{j+1\sigma}c_{j\sigma}] + U\hat{D} \qquad (4)$$

where $c^+_{j\sigma}$ ($c_{j\sigma}$) is the creation (annihilation) operator for an electron with spin σ at site j, which is described by the wave function $\phi(x - x_j)$ and $\hat{D}$ is the double occupancy operator given by:

$$\hat{D} = \sum_j n_{j\uparrow} n_{j\downarrow}; \quad n_{j\sigma} = c^{+}_{j\sigma} c_{j\sigma} \qquad (5)$$

3. VARIATIONAL STUDY OF THE PLASMA FREQUENCY AND SPIN MAGNETIC SUSCEPTIBILITY FOR ARBITRARY ELECTRON DENSITY.

The Hubbard Hamiltonian is a many-body model which is easier to handle than the complete Hamiltonian including the long-range forces of the Coulomb interactions, but still very difficult to diagonalize. In fact, this has only been achieved for a half-filled one-dimensional lattice [10]. For $n \neq 1$ the one-dimensional model was not fully solved but reduced to a system of coupled integral equations [10].

The variational ansatz introduced by Gutzwiller [6] is defined by:

$$|\phi> = e^{-[\eta \hat{D}]/2} |\phi_{SL}> \qquad (6)$$

where $|\phi_{SL}>$ is the Slater determinant which describes the ground state of (4) for $U = 0$ and η is a variational parameter.

The application of the exponential operator of the r.h.s. of Eq. (6) on the ground state wave function $|\phi_{SL}>$ reduces the weight of the configurations having doubly occupied sites.

According to the variational principle of quantum mechanics, the best approximation for the ground state energy is obtained by minimizing the functional

$$E = \frac{<\phi|\hat{H}|\phi>}{<\phi|\phi>} \qquad (7)$$

which leads to $\eta = 0$ for $U = 0$ and $\eta \to \infty$ for $U \to \infty$. We restrict the present study to the small U regime, i.e. $u = U/4t \leq 1$. The use of the quantum mechanics machinery allows the evaluation of a small η expansion of the energy (7). The detailed calculation is presented in reference [11]. After energy minimization we arrive at:

$$E = E_{HF} + E_{corr}$$

$$E_{HF}/\, t\, N_a = -\frac{4}{\pi} \sin k_F + u\left[\frac{2 k_F}{\pi}\right]^2 \qquad (8)$$

where E_{HF} denotes the energy obtained by the usual Hartree-Fock approximation and the correlation energy E_{corr} reads:

$$E_{corr}/t\, N_a = -u^2 \frac{4 k_F^4}{\pi} \frac{(1 - \frac{4 k_F}{3\pi})^2}{(\sin k_F)[k_F(\pi - k_F) + \sin^2 k_F]} \qquad (9)$$

As the kinetic energy T is related to the ground state energy (7) by $T = t\, dE/dt$ [8], we obtain:

$$|T|/t\, Na = \frac{4}{\pi} \sin k_F \left[1 - u^2 \frac{k_F^4 (1 - \frac{4 k_F}{3\pi})^2}{(\sin^2 k_F)[k_F(\pi - k_F) + \sin^2 k_F]}\right] \qquad (10)$$

The function (10) decreases monotonically with U for all densities. For the half-filled band case Eq. (10) reads:

$$|T| / t N_a = \frac{4}{\pi} [1 - 0.1951 u^2] \qquad (11)$$

This result is in good agreement with the Bethe ansatz expansion of Reference [12], covering 91.4% of the exact coefficient.

As we have already mentioned, experimental data show that the plasma frequency as determined by the partial sum rule (involving all intraband transitions) [2] is rather sensitive to correlation effects, decreasing for increasing values of the Coulomb effective repulsion.The square of the plasma frequency is proportional to the f-sum rule, which for the one-dimensional Hubbard model is simply proportional to the absolute value of the mean kinetic energy [8]. Thus the variational result (10) supports the experimental evidence that the oscillator strength of optical absorption of the synthetic quasi-one-dimensional metals is depressed by correlations. On the other hand, experimental data indicate an enhancement of the magnetic susceptibility for increasing values of the effective Coulomb repulsion [2], [3].

The magnetic susceptibility for the one-dimensional Hamiltonian (4) has been calculated exactly for the half-filled band case [13].

The main purpose of the present paper is to use the variational wave function (6) to derive a small U expansion for the spin magnetic susceptibility when $n \neq 1$. Applying a magnetic field to the electronic system described by (4), a small U energy expansion of the r.h.s. of Eq. (7) can be evaluated by the method described in [11] for zero magnetic field.

We omit here the details of the calculations, which are more involved than the ones of Reference [11] because of the magnetization dependence of the energy. Nevertheless, although the free propagators depend now on the spin indices, the diagrams which contribute to the correlation energy are the same as in the zero magnetic case.

The small U spin magnetic susceptibility expansion derived from the variational wave function (6) reads:

$$\chi = \chi_0 \{ 1 + u_F^2 + u_F [1 - J(k_F) [1 - J(k_F) G(k_F)]] \} \qquad (12)$$

where $\chi_0 = \mu_0^2 / (\pi t \sin(k_F))$ is the Pauli susceptibility of the non interacting system, $u_F = U/(2\pi t \sin(k_F)) < 1$ and

$$J(x) = \frac{(x\pi)^2 \ (1 - \frac{4x}{3\pi})}{\sin^2 (x) + x (\pi - x)} \qquad (13)$$

$$\pi^2 G(x) = 1 + \frac{1}{4} [\sin^2 (x) + x(\pi - x)] + (\frac{\pi}{2} - x) \cot (x) \qquad (14)$$

The magnetic susceptibility (12) is represented in figure 1 as a function of u for

fixed values of carrier density. χ is enhanced by correlation effects, and this effect is more pronounced for smaller values of band filling. A detailed comparison with the numerical results of Shiba [14] is difficult because our results are restricted to small u values. Nonetheless the curves of the figure agree qualitatively with his results. As expected, the magnetic susceptibility is enhanced by correlations for all carrier densities.

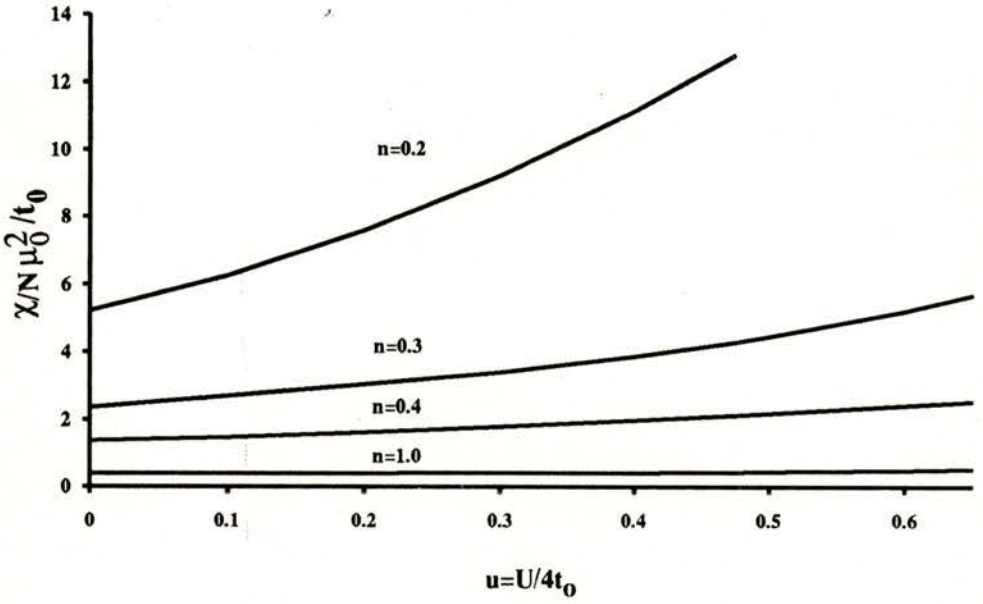

Fig.1:Magnetic Susceptibility as a function of u for different values of the electronic density as given by the Gutzwiller wave function.

4. CONCLUSION

In this paper we have studied the ground state properties of the Hubbard chain by means of the variational Gutzwiller ansatz. Our results are restricted to the small U regime, but arbitrary density n. The main aim of the paper is to show that, in addition to a decrease of the plasma frequency as determined from the

partial sum rule [8], the Gutzwiller wave function predicts that the electronic correlations lead to an enhancement of the magnetic susceptibility for all densities n>0, in agreement with the experimental data for organic synthetic metals [2], [3].

Another typical effect of the electronic correlations in these materials, which has also been detected experimentally [15], is the occurrence of phonon diffuse X-ray scattering at $4\,k_F$.

The study of this problem requires the introduction of the electron-phonon coupling, which is out of the scope of the present work. A generalization of the present variational method to the study of the effects of the electronic correlations on the electron-phonon interaction is in preparation.

ACKNOWLEDGEMENTS

We are very much indebted to Professors Bessa Sousa and Leite Videira for encouragements. J. C. would like to thank Professor Baeriswyl for discussions and introduction of the problem treated in this work.

REFERENCES

[1] Ferraris, J., Cowan, D., Walatka, V. and Perlstein, J., J. Am. Chem. Soc. 95, 948 (1973).

[2] Jacobsen, C., Johannsen, I. and Bechgaard, K., Phys. Rev. Lett. 53, 194 (1984).

[3] Jérome, D. and Schultz, H. J., Adv. Phys. 31, 299 (1982).

[4] Bednorz, J. G. and Müller, K. A., Z. Phys. B, 64, 189 (1986).

[5] Hubbard, J., Proc. Roy. Soc. London, sec A 276, 238(1963); 277, 237 (1964).

[6] Gutzwiller, M., Phys. Rev. Lett. 10, 159 (1963); Phys. Rev. 134, A923 (1964); 137, A1726 (1965).

[7] Carmelo, J. and Micnas,R., J. Phys.: Cond. Matter 2, 6981 (1990).

[8] Baeriswyl, D., Carmelo, J. and Luther,A., Phys. Rev. B 33, 7247 (1986); 34, 8976 (1986).

[9] Mazundar, S. and Bloch, A., Phys. Rev. Lett. 50, 207 (1983).

[10] Lieb, E. and Wu, F., Phys. Rev. Lett. 20, 1445 (1968).

[11] Carmelo, J., Dzierzawa, M., Zotos, X. and Baeriswyl, D., Phys. Rev. B 43, 598 (1991).

[12] Carmelo, J. and Baeriswyl, D., Phys. Rev. B 37, 7541 (1988).

[13] Takahashi, M., Progr. Theor. Phys. 42, 1098 (1969); 43, 1619 (1970).

[14] Shiba, H., Phys. Rev. B 6, 930 (1972).

[15] Pouget, J. P., Khanna, S. K., Denoyer, F. and Comès, R., Phys. Rev. Lett. 37,437 (1976).

MESONIC COUPLINGS IN THE NAMBU-JONA-LASINIO MODEL. THE $\sigma \rightarrow \pi\pi$ DECAY

M. C. RUIVO
Centro de Física Teórica Departamento de Física da Universidade de Coímbra, 3000 Coímbra
Portugal

ABSTRACT-A technique to calculate the coupling between mesons, in the framework of the Nambu-Jona-Lasinio model is proposed. The approach is based on the Time Dependent Hartree-Fock Theory and consists of a boson expansion including appropriate anharmonic terms. The technique is applied to the calculation of $g_{\sigma\pi\pi}$, for the bound state solution as well as for the discretized solutions of the $q\bar{q}$ continuum. The physical meaning of these solutions is discussed.

1. INTRODUCTION

The interpretation of the mesonic spectrum in terms of the underlying dynamics of strong interactions is nowadays an important issue in particle physics. Both the difficulties of experimental identification of those mesons and the controversy about their quark structure show that many questions remain open [1],[2]. Different approaches have focused on the scalar meson problem. Besides the conventional description of those mesons as $q\bar{q}$ states, which does not allow to fit all the data available, interpretations of their structure as multiquark states, glueballs or suitable combinations of those states have been explored [2],[3],[4],[5],[6],[7],[8]. The work here reported is part of a program of investigation of meson properties within the framework of the Nambu-Jona-Lasinio (NJL) model [9] where the mesons are taken as $q\bar{q}$ excitations. The approach, based on the conventional Time Dependent Hartree-Fock (TDHF) formalism, as developed to deal with non-relativistic nuclear structure situations, explores the analogy between the model and a many-body system of non-relativistic fermions [10]. The aim of the present work is, in the first place, to present a bosonization technique, which takes into account anharmonic terms responsible for the couplings between mesons. The technique is here used to calculate the decay of the scalar-isoscalar mesons into two pions, within the framework of a $SU(N_f = 2)$ NJL model and applied to the bound state solution as well as to the discretized solutions of the

$q\bar{q}$ continuum. We hope to provide, in this way, some physical insight on the discretization of the continuum. This version of the model is, certainly, too simple to provide a realistic description of the scalar mesons and we do not expect, in this preliminary work, to obtain accurate quantitative results. The technique proposed might, however, be applied to more sophisticated schemes and to the decay of other mesons.

The NJL model is described by an effective Lagrangian of relativistic fermions interacting through a two-body contact force. The gluonic degrees of freedom are assumed to be frozen. The model, which incorporates the basic symmetries of QCD and satisfies the relevant current algebra relations, provides an useful tool to investigate the low energy region of the hadronic spectrum. For zero current quark masses it allows for the description of the mechanism of dynamical chiral symmetry breaking, which leads to a vacuum of $q\bar{q}$ condensates associated with the emergence of massless collective excitations of $q\bar{q}$ with the quantum numbers of pseudoscalar isovector mesons (the Goldstone pions) and with the occurrence of a mass of dynamical origin for the constituent quarks. Excitations of $q\bar{q}$ states, with proper quantum numbers of mesons, may be extracted from the new vacuum.

Although the pion sector is well described within the original versions of the model, problems with the description of the other mesons lead, for instance, to the construction of generalized versions [11,12]. Interest in the excitation modes of the NJL model was restricted, until recently, to bound states. Although the existence of the modes of the continuum was recognized, they were commonly disregarded. As a matter of fact, unless a confining mechanism is implemented in the model, unbound states would decay into $q\bar{q}$ pairs, being considered as unphysical. However, recently these modes have been object of interest [13,14,15,16]. In [13] a method for obtaining the solutions of the NJL model by means of a polynomial ansatz was proposed. This method leads to a discretization of the continuum and is equivalent to introducing a constraint on the $q\bar{q}$ relative motion. This might be faced as a modification of the original NJL model, in which effects of a confining mechanism are incorporated. The same mechanism was recently implemented in the framework of an extended NJL model [14]. The results obtained for the meson spectrum are in good qualitative agreement with experience, providing, therefore, support for the interpretation of the mesonic excitations of the continuum.

The calculation of the decay amplitudes of those modes is an essential piece of information for a possible identification with physical resonances. In the present work we propose a method to calculate these quantities.

This investigation is carried out within the framework of a TDHF formalism for the NJL model. Previously, this formalism was implemented in the small

amplitude limit of the mean field description leading to linearized equations of motion for the excitation modes, equivalent to the Random Phase Approximation (RPA) equations [10]. In this approximation the coupling between the normal modes is neglected but the effects of such couplings might be taken into account through adequate inclusion of anharmonic terms. The bosonization technique for calculating the $\sigma\pi\pi$ coupling is an extension of the previous treatment, consisting in enlarging the expansion of the effective Lagrangian in order to include anharmonic terms associated with the $\sigma\pi\pi$ coupling [17]. An analogous role of anharmonicities in the damping of giant resonances of many-body systems is considered in [18].

We start with a brief review of the model and formalism and of the concepts involved in the discretization of the continuum. Then we present the description of the method for calculating $g_{\sigma\pi\pi}$. The calculation of the decay amplitude for different solutions of scalar modes follows straightforwardly. Finally, the results are discussed.

2 DESCRIPTION OF THE METHOD

2.1 Review of the Formalism.

The dynamics of a many-body interacting system within TDHF formalism is described by a Hamiltonian of the generic form:

$$H = \sum_{i=1}^{N} t(i) + 1/2 \sum_{i\neq j} v(i,j) . \qquad (1)$$

We write, therefore the Hamiltonian of the NJL model as:

$$H = \sum_{i=1}^{N} [\gamma_5 (i)\sigma(i).\mathbf{p}_i + \beta(i)m_0]$$

$$-g\sum_{i\neq j} \delta (\mathbf{x}_i - \mathbf{x}_j) \beta(i) \beta(j) [I - \gamma_5 (i) \gamma_5 (j) \tau(i).\tau(j)] \qquad (2)$$

where m_0 is a small current quark mass ($m_u = m_d = m_0$), the τ^a (a = 1,2,3) are the $SU(N_f = 2)$ generators, β, γ_5 and $\gamma_5\sigma$ are Dirac matrices and g is the coupling constant. The Hamiltonian (2) is left invariant under a chiral rotation in the γ_5 -isospin space, if $m_0 = 0$. The vacuum state is described by a Slater determinant of negative energy states, $|\phi_0>$, with momentum lower than a cutoff Λ, or, equivalently, in terms of the HF density matrix:

$$\rho_0 = 1/2 [I - (\beta M + \gamma_5\sigma.\mathbf{p})/E] \theta (\Lambda^2 - p^2) , \quad (3)$$

where $E=(p^2+M^2)^{1/2}$ and M is a variational parameter interpreted as the mass of the constituent quarks, which is given by the gap equation:

$$1 - m_0/M = 26g \sum_{p} \frac{\theta(\Lambda^2 - \pi^2)}{E} . \qquad (4)$$

This equation was obtained by minimizing with respect to M the functional of the energy:

$$\varepsilon[\rho] = tr_1\, \rho(1)\, t(1) + \frac{1}{2} tr_1 tr_2\, \rho(1)\rho(2) v^A(12), \qquad (5)$$

where v^A (12) is the antisymmetrized two-body interaction.

Deviations from the state of equilibrium lead to a deformed state $|\phi\rangle = U\,|\phi_0\rangle$, which may also be described in terms of the general density matrix $\rho = U\,\rho_0\,U^+$, where U is an unitary time-dependent operator. The time evolution of the system may be derived from the Lagrangian:

$$\underline{\underline{L}}^{(2)} = itr\,(\dot{U}\rho_0 U^+) - \varepsilon[\rho]. \qquad (6)$$

Choosing $U = \exp(iS)$, where S is a hermitian single particle time-dependent operator, and assuming that the fluctuations around the equilibrium configuration are small, the Lagrangian may be expanded up to second order in S, leading to

$$\underline{\underline{L}}^{(2)} = \frac{i}{2}\langle\phi_0|[S,\dot{S}]|\phi_0\rangle - \frac{1}{2}\langle\phi_0|[S,[H,S]]|\phi_0\rangle \qquad (7)$$

By making use of the action principle, performing arbitrary variations with respect to the variational functions contained in S and assuming harmonic dependence on time, one obtains homogenous linearized equations of motion, equivalent to the RPA equations.

2.2 Discretization of the continuum

The mesonic excitations of the vacuum below the $q\bar{q}$ threshold (E_{th}=2M), investigated in [10], are solutions of exact RPA equations. The same treatment might easily be used to explore the region above the threshold ($q\bar{q}$ continuum). This region was, until recently, considered as not worthy of interest, due to the lack of confining mechanism in the model. However, as it is well-known, there is some strength which is not exhausted by the bound state solutions and is localized in the continuum, as explained in [13]. Information concerning meson properties should, therefore, lie also in the continuum of the model. The question is how this information can be extracted.

This region was studied, within the framework of the formalism described above, using a technique which discretizes the continuum [13]. The basis of the technique is very simple and consists in replacing the variational functions of the generators of the fluctuations, which are generic functions of **p**, by low order of polynomials. By using polynomials of the form $a + bp^2$, two discrete solutions of the RPA equations are obtained: one replaces the bound state solution and the other the continuum. The constraint imposed in the momentum space reduces the infinite number of continuum modes to one single mode, in an analogous way to what would be expected from a confining mechanism. In the modified model large values of the $q\bar{q}$ distance are forbidden. The masses obtained in this

way for the low-lying mesons are in good agreement with experiment. The lowest pseudoscalar-isoscalar mode always appears at zero energy, in the chiral limit, and small deviations of the current algebra relations are obtained.

An exact and covariant treatment of the $q\bar{q}$ continuum of a $SU(N_f = 2)$ NJL model is reported in [15]. The masses of the mesons are identified with the center of gravity of the strength distribution. In [16] the continuum modes are also studied in the context of a generalized NJL model.

All these approaches call for the attention of the continuum modes and predict values for their masses. In order to clarify its physical meaning one should look at their decays. One could regard the decay of the continuum modes through two different mechanisms:

-The Landau damping of the exact solutions, which means that the collective $q\bar{q}$ modes spread its strength over a multitude of continuum normal modes and lose their identity due to interference effects. This does not correspond, in the original NJL model, to the true physical decay. This mechanism is prevented to occur in the modified model by our choice of the generating functions.

-The two-body damping of the discretized solutions in few normal modes, which we regard as the true physical decay.

In order to calculate the decay amplitude of the resonances in specific channels one should implement the mechanism analogous to the two-body damping in many-body systems. This is achieved by performing an adequate bosonization of the original Hamiltonian, including anharmonic terms which are responsible for the decay of the normal modes.

The bosonization technique described below is applied to the calculation of the decay of the exact bound state and of the discretized solutions of scalar-isoscalar mesons into $\pi\pi$. Convenient adaptations of the same technique might be used to calculate other decays.

This will also allow to clarify the meaning of the discretization technique, which should by no means be regarded as an approximation in order to avoid the exact RPA treatment (which, anyway, does not present particular difficulties) but as a device to incorporate effects of confinement.

2.3 Bosonization technique and calculation of $g_{\sigma\pi\pi}$

Bosonization is nothing more than an identification of canonical coordinates. As is well-known, the RPA approximation is the lowest order of a boson expansion which maps a fermion subspace into a boson subspace, the HF vacuum, $|\phi_0>$, being mapped into the RPA vacuum, $|\ >$, and the fermion operators into boson operators. In the present case we are interested in an expansion in boson operators (canonical coordinates) up to third order. We start by expanding the functional of the energy $\varepsilon[\rho]$ in powers of S up to this order:

$$\varepsilon[\rho] = \langle\phi|H|\phi\rangle \simeq \langle\phi_0|H|\phi_0\rangle + \frac{1}{2}\langle\phi_0|[S,[H,S]]|\phi_0\rangle + \frac{i}{3!}\langle\phi_0|[S,[S,[S,H]]]|\phi_0\rangle, \quad (8)$$

In order to make a connection with the RPA formalism it is convenient to write the generator of the fluctuations of the vacuum as:

$$S = \sum_{\tau} (\alpha_\tau \Theta_\tau e^{i\omega_\tau t} + \alpha_\tau^* \Theta_\tau^+ e^{-i\omega_\tau t}) \quad (9)$$

where ω_τ is the frequency of a generic mode of excitation τ and Θ_τ , (Θ_τ^+) are one-body fermion operators. These operators may be normalized by imposing the condition:

$$\langle\phi_0|[\Theta_\tau , \Theta_\tau^+]|\phi_0\rangle = 1 , \quad (10)$$

The variables α_τ and α_τ^* are canonical coordinates. Expanded in these variables, the harmonic terms describe the energy of the modes and the anharmonic (third order terms) describe their decays. The harmonic term of the functional of the energy can be written as:

$$\varepsilon^{(2)} (\alpha_\tau^* , \alpha_\tau) = \omega_\tau \alpha_\tau^* \alpha_\tau \quad , \quad (11)$$

with:

$$\omega_\tau = \langle\phi_0|[\Theta_\tau , [H , \Theta_\tau^+]]|\phi_0\rangle, \quad (12)$$

The harmonic RPA effective Hamiltonian may, therefore, be written as

$$\hat{H} = \omega_\tau A_\tau^+ A_\tau , \quad (13)$$

where A_τ^+ (A_τ) are boson operators.

In order to calculate $g_{\sigma\pi\pi}$ we need the appropriate anharmonic perturbation. Writing $S = S_\sigma + S_\pi$, and taking advantage of the form of the generator S (9), we easily obtain the component of the third order term, relevant for describing the process $\sigma - \pi\pi$:

$$\varepsilon_{\sigma\pi\pi} = \lambda_{\sigma\pi\pi} (\alpha_\sigma \alpha_\pi^* \alpha_\pi^* + \alpha_\pi \alpha_\pi \alpha_\sigma^*) , \quad (14)$$

with:

$$\lambda_{\sigma\pi\pi} = \frac{i}{3!}\langle\phi_0|[\Theta_\sigma,[\Theta_\pi^+,[\Theta_\pi^+,H]]] + [\Theta_\pi^+,[\Theta_\sigma,[\Theta_\pi^+,H]]] + [\Theta_\pi^+,[\Theta_\pi^+,[\Theta_\sigma,H]]]|\phi_0\rangle , \quad (15)$$

By definition, $g_{\sigma\pi\pi}$ is given by:

$$g_{\sigma\pi\pi} = \lambda_{\sigma\pi\pi} \sqrt{2\omega_\sigma}\, (2\omega_\pi) , \quad (16)$$

In order to describe a process in which one σ at rest decays into two pions with opposite momenta, one should have a perturbation Hamiltonian of the form:

$$W = \sum_{k} \frac{1}{2} \lambda_{\sigma\pi\pi} (k) (B^+ A_k A_{-k} + A_{-k}^+ A_k^+ B), \quad (17)$$

where W is the effective interaction RPA Hamiltonian and $B^+(B)$, $A_{-k}^+(A_k)$ are creation (annihilation) operators, respectively for σ and π.

Here we take the following approximation:

$$\lambda_{\sigma\pi\pi}(\mathbf{k}) \simeq \frac{g_{\sigma\pi\pi}}{\sqrt{2\omega_\sigma\,(2\omega_\pi(\mathbf{k}))}} \quad . \qquad (18)$$

The transition amplitude is easily obtained through the Fermi Golden rule. In the chiral limit we have:

$$\Gamma_{\sigma\pi\pi} = \frac{3|g_{\sigma\pi\pi}|^2}{16\pi\omega_o}\left(1 - \left(\frac{2\omega_\pi}{\omega_\sigma}\right)^2\right)^{1/2} \qquad (19)$$

where the factor 3 comes from isospin degeneracy. The calculation of $\lambda_{\sigma\pi\pi}$ from (15) is straightforward. Bearing in mind that, within our formalism the pseudoscalar-isovector modes and the scalar-isoscalar modes are described, respectively, by the generators:

$$S_\pi^a = [\gamma_5 L_1 + i\,\beta\gamma_5 L_2]\tau^a \,, \quad a = 1,2,3 \qquad (20)$$

$$S_\sigma = \gamma_5\,\sigma.\pi F_1 + i\,\beta\gamma_5\,\sigma.\pi F_2 \,, \qquad (21)$$

where L_i and F_i (i=1,2) are variational functions depending on p^2 and t, one obtains:

$$\lambda_{\sigma\pi\pi} = 48\, M_* 26\, g \Big[\sum_p \frac{p^2 F_2}{E}\,\Theta|\Lambda^2 - p^2| \sum_p \frac{L_1^{*2} + L_2^{*2}}{E}\,\Theta|\Lambda^2 - p^2|$$

$$- \sum_p \frac{L_1^*}{E}\,\Theta|\Lambda^2 - p^2| \sum_p \frac{p^2}{E}(F_2 L_1^* + F_1 L_2^*)\,\Theta|\Lambda^2 - p^2| \Big] \qquad (22)$$

The variational functions L_i and F_i were taken as the eigenvectors of the RPA equations of previous works [10,13]. The numerical values were calculated in the chiral limit.

3. DISCUSSION OF THE RESULTS

We show in Table 1. numerical values for ω_σ, $g_{\sigma\pi\pi}$ and $\Gamma_{\sigma\pi\pi}$, obtained, respectively, for the bound state solution and for the discretized solutions of σ decaying into two pions for $\lambda = 2M$ and different values of M. These input parameters obey the self-consistent equation and were chosen so that the quantities $< \bar{\Psi}\Psi >$ and f_π are in the range of its empirical values (see [10]). The numerical values shown are the result of an improved calculation, in relation to those included in [17]. The calculation of $g_{\sigma\pi\pi}$ for $\Omega_\sigma = 2M$ is useful as a check to our method. This decay has already been calculated by other authors using different techniques [19],[20] The value obtained for the decay width does not allow to identify this solution with an established physical particle. The problem of assigning a physical meaning to this solution is related with the controversial existence of a scalar-isoscalar meson with a mass below

700 MeV. The behaviour of this solution with temperature [19] and density [20] was already discussed.

Table 1.

	Conv. RPA			Const. RPA		
M (MeV)	ω_σ (MeV)	$\lvert g_{\sigma\pi\pi}\rvert$ (MeV)	$\Gamma_{\sigma\pi\pi}$ (MeV)	ω_σ (MeV)	$\lvert g_{\sigma\pi\pi}\rvert$ (MeV)	$\Gamma_{\sigma\pi\pi}$ (MeV)
335	670	2861	660	716	3986	1184
				1269	1350	84
350	700	2989	693	748	4112	1242
				1326	1410	87

Table 1. ω_σ, $\lvert g_{\sigma\pi\pi}\rvert$ and $\Gamma_{\sigma\pi\pi}$ for solutions obtained with the conventional RPA and the constrained RPA.

The results for the couplings and decay widths of the modes obtained through the discretization technique are new and require further consideration.

As it was already mentioned, the polynomial ansatz leads to two modes, one replacing the exact bound state solution and the other replacing the continuum modes. The results obtained for the masses and decay widths support this interpretation. The comments made before concerning the solution $\omega_\sigma = 2M$ apply to the first mode. The value obtained for the decay width is in agreement with the lack of experimental evidence for a resonant behaviour in the scalar-isoscalar channel in the region of 600 - 700 MeV [1]. The second mode might be interpreted as a low-lying scalar-isoscalar meson. The two lowest established scalar-isoscalar resonances are the $f_0(975)$ with decay amplitude Γ = 34 MeV (75% into $\pi\pi$ and 25% into $K\bar{K}$) and the $f_0(1400)$ with Γ = 150 - 400 MeV ($\simeq$ 90% into $\pi\pi$ and $\simeq$ 10% into $K\bar{K}$) [1]. Although a $SU(N_f = 2)$ model cannot provide a realistic description any of those mesons, which have a component of strangeness, the $f_0(975)$ is more unlikely described by this version of the model (even at a qualitative level). A description of this meson as a $q\bar{q}$ state, even allowing for flavour mixing, is often considered unsuitable to account for its properties (namely its branching ratio into $K\bar{K}$ (25%), in spite of the small phase space available). Interpretations of this meson as a $K\bar{K}$ molecule seems more appropriate, while the $f_0(1400)$ is more commonly interpreted as a true resonance [1,6,21]. In view of this situation it seems reasonable to compare the present results for the second mode to the $f_0(1400)$.

Moreover, the numerical values obtained provide support to this comparison. We notice, however, that our value for the decay width is low compared to the estimated experimental value of the $f_0(1400)$.

The present results should be regarded as essentially qualitative. The main point is that we show that it is possible to implement a mechanism through which the discretized modes of the continuum can decay in specific meson channels. The bosonization technique, together with the polynomial ansatz, makes possible a consistent treatment of the modes of the continuum. The investigation of the effect of giving to the scalar mesons a more complex structure in the framework of a generalized NJL model and the improvement of the present technique, are feasible within the TDHF formalism. Research along these lines is being carried out.

ACKNOWLEDGEMENTS

I would like to thank J. da Providência, M. K. Banerjee, C. A. de Sousa, B. Hiller and A. H. Blin for helpful discussions. This work was supported by Instituto Nacional de Investigação Científica.

REFERENCES

[1] Particle Data Group, Phys. Lett. **B239**, 1 (1990).

[2] Diekmann, B., Phys. Rep. **159**, 99 (1988).

[3] Sharpe, S. R., Jaffe, R. L. and Pennington, M. R., Phys. Rev. **D30**, 1013 (1984).

[4] Teshima, T. and Oneda,S., Phys. Rev. **D33**, 1974 (1986).

[5] Estabrooks, P., Phys. Rev. **D19**, 2678 (1979).

[6] Weinstein, J. and Isgur, N., Phys. Rev. **D27**, 588 (1983) and Phys. Rev. **D41**, 2236 (1990).

[7] Mennessier, G., Narison, S. and Paver, N., Phys. Lett. **B158**, 153 (1985).

[8] Au, K. L., Morgan, D. and Pennington, M. R., Phys. Rev. **D35**, 1633 (1987) and Phys. Lett. **B167**, 229 (1986).

[9] Nambu, Y. and Jona-Lasinio, G., Phys. Rev. **122**, 345 (1961) and Phys. Rev. **124**, 246 (1961).

[10] da Providência, J., Ruivo, M. C. and de Sousa, C. A., Phys. Rev. **D36**, 1882 (1987) and Phys. Rev. **D38**, 2646 (1988); de Sousa, C. A., Z. Phys. **C43**, 503 (1989).

[11] Ebert, D. and Reinhardt, H., Nucl. Phys. **B271**, 188 (1986).

[12] Bernard, V. and Meissner, U. G., Nucl. Phys., **A489**, 647 (1988).

[13] da Providência, J. and de Sousa, C. A., Phys. Lett. **B237**, 147 (1989).

[14] de Sousa, C. A., Z. Phys. C **49,** 619 (1991)

[15] Blin, A. H., Hiller, B. and da Providência, J., Phys. Lett. **B241**, 1 (1990).

[16] Klimt, S., Lutz, M., Vogl, U. and Weise, W., Nucl. Phys. **A516**, 429 (1990).

[17] Ruivo, M. C., Europhys. Lett., **15**, 139 (1991) [18] da Providência, J., Europhys. Lett. **4**, 789 (1987).

[19] Hatsuda, T. and Kunihiro, T., Phys. Lett. **B185**, 304 (1987) and Prog. Theor. Phys. **91**, 248 (1987).

[20] Bernard, V., Meissner, U. G. and Zahed, I., Phys. Rev. Lett. **59**, 966 (1987).

[21] Lohse, D., Durso, J. W., Holinde, K. and Speth, J., Nucl. Phys. **A516**, 513 (1990).

CONTENTS

AUTHOR INDEX

Processamento de Texto: Hugo S. Sanches

Impressão e Acabamento: Imprensa Portuguesa — PORTO

SOCIEDADE PORTUGUESA DE FÍSICA
AV. REPÚBLICA 37-4.°, 1000 LISBOA, PORTUGAL

PORTUGALIAE PHYSICA publishes articles or research notes with original results in theoretical, experimental or applied physics; invited review articles may also be included.

Manuscripts, with an abstract, may be written in English or French; they should be typewritten with two spaces and in duplicate. Figures or photographs must be presented in separate sheets and be suitable for reproduction with eventual reduction in size; captions should make the figures intelligible without reference to the text. Authors are requested to comply with the accepted codes concerning references.

There is no page charge. Author(s) will get 50 free reprints (without covers); these are to be shared among all the authors of the article. Authors interested in more reprints should say so when sending their manuscripts; quotations shall be sent with the proofs.

Subscription rates for volume 20:

3.600 Escudos (US$24) — individuals
9.000 Escudos (US$60) — libraries

PORTUGALIAE PHYSICA may also be sent on an exchange basis; we welcome all suggestions to such effect.

All mail to be addressed to

PORTUGALIAE PHYSICA

C/O LABORATÓRIO DE FÍSICA, FACULDADE DE CIÊNCIAS
PRAÇA GOMES TEIXEIRA
4000 PORTO PORTUGAL

PORTUGALIAE PHYSICA

VOL. 20 • 1989 / 91

CONTENTS

ISSN 0048-4903 PORYAA 20 1-63 (1989/91)